Crystallization kinetics of repulsive colloidal spheres

1999 J. Phys.: Condens. Matter 11 R323

(http://iopscience.iop.org/0953-8984/11/28/201)

J. Phys.: Condens. Matter **11** (1999) R323–R360. Printed in the UK PII: S0953-8984(99)83007-0

REVIEW ARTICLE

Crystallization kinetics of repulsive colloidal spheres

Thomas Palberg

Institut für Physik, Johannes Gutenberg Universität Mainz, Staudingerweg 7, D-55099 Mainz, Germany

Received 4 December 1998, in final form 15 April 1999

Abstract. Colloidal spheres interacting via a purely repulsive potential provide an excellent model system to study the kinetics of solidification from the melt. Such systems are readily accessible by comparably simple yet powerful optical methods like time resolved static light scattering and microscopy, reviewed in the first part of this paper. We then present results from our own recent studies within a framework of data available from literature. In particular we investigated nucleation and growth of hard sphere crystals using combined Bragg and small angle light scattering and of charged sphere crystals using Bragg microscopy. Special attention is given to the range of validity of classical nucleation theory and of Wilson Frenkel growth and a discussion of kinetic prefactors for both processes.

1. Introduction

The kinetics of crystallization are a long standing fundamental problem in condensed matter physics [1]. Although considerable progress has been achieved through the use of novel or refined experimental techniques [2–4], theoretical efforts and computer simulations [5, 6], and the study of model systems [7–9] a comprehensive understanding is still lacking. In this review the focus is on recent work with colloidal model systems well suited to investigate the kinetics of freezing, i.e. suspensions of spherical particles interacting via a purely repulsive potential. In these significantly different boundary conditions are encountered, while the underlying physics are much the same as in atomic or molecular melts [10, 11]. For several reasons colloidal systems are excellently suited to study the basic phenomena of solidification. However, the final success of such studies and the gained improved understanding is aimed at the transfer of concepts back to atomic systems and forward towards the design of new materials [12, 13]. The paper is organized as follows. The next section gives a short motivating outline of the relevant similarities and differences between colloidal and atomic systems. The third section introduces a variety of optical methods employed to study colloidal crystallization kinetics with a special emphasis on scattering methods. In the fourth and fifth sections experiments on hard and charged sphere suspensions are presented, and compared to data from literature and theoretical concepts.

2. Colloidal suspensions as model systems for solidification experiments

The analogy between atomic and colloidal fluids, crystals and glasses often allows us to address the latter as conveniently enlarged model system of the former. To show this we first take a look at the phase behaviour of both kinds of system from a more theoretical point of view. In general, liquids subjected to temperatures below their freezing temperature or to pressures

0953-8984/99/280323+38$30.00

larger than their freezing pressure will undergo a first order phase transition to the crystalline state. Likewise crystallization occurs from supersaturated solutions. Attraction in the pair interaction or in the potential of mean force generally plays an important role as it introduces large density differences between disordered and ordered phases. However, it became clear from theoretical arguments that attraction in the first place generates van der Waals-like loops in the pressure–density phase diagram. Thus stable liquids are formed in the temperature range between the triple temperature and critical temperature [14, 15]. Interestingly, by tuning the range and amplitude of the attraction as compared to the repulsion the position of the critical point may be shifted into the fluid–solid coexistence regime or even on the solid side [16–18]. The somewhat counter-intuitive prediction then is the absence of a liquid phase—as for C_{60} [19]—or the appearance of a symmetry conserving solid–solid phase transition. It was also found that for one component systems repulsion alone is sufficient to induce ordering (see e.g. [20]) and that the phase transition shifts to lower densities if the repulsion between particles is enhanced. Two prominent examples are the entropy driven crystallization of hard spheres (HSs) leading to face centred cubic (fcc) crystals [21] and the one component plasma (OCP) undergoing Wigner crystallization into body centred cubic (bcc) lattices, if the interaction parameter $\Gamma \geqslant 178$.

Colloidal fluids on the other hand will undergo crystallization at constant temperature and ambient pressure, if the interaction between the particles becomes large enough [11, 22, 23]. In the case of HS suspensions the packing fraction Φ is the only relevant parameter [24, 25]. Charged spheres (CSs) interact via a screened Coulomb potential. There in addition to the number density of particles $n = 3\Phi/4\pi a^3$—where a is the particle radius—the particle charge and the concentration of screening electrolyte c can be used to adjust the strength and steepness of the repulsion over a wide range between the theoretical limits of HS and OCP [26]. So-called depletion attraction may be introduced into the potential of mean force by adding a second component [27, 28]. This may be a non-adsorbing polymer, a polyelectrolyte or a second kind of much smaller particle. Recent theoretical work seems to indicate that under some conditions also the small ions present in charged systems may induce such an attraction [29]. In most cases it leads to a competition between phase separation and ordering kinetics which is of great practical relevance e.g. in the crystallization of proteins. It, however, introduces a number of further complications and also only few experimental data are as yet available [30]. In this review therefore only purely repulsive systems are considered in detail.

Secondly the kinetics of crystallization in both atomic and colloidal systems are controlled by the exponential dependence on the ratio between some intrinsic energy scale and the thermal energy $k_B T$. From this observation the classical rate equations result which for instance give the nucleation rate density J as:

$$J = J_0 \exp(-\Delta G^*/k_B T) \tag{1}$$

where ΔG^* is the height of the nucleation barrier and J_0 a kinetic prefactor [5, 31, 32]. Reaction limited growth velocities should follow a Wilson–Frenkel (WF) type behaviour [33]:

$$v = v_\infty[1 - \exp(-\Delta\mu/k_B T)] \tag{2}$$

where v_∞ is the limiting velocity for infinite chemical potential difference $\Delta\mu$ between melt and solid. In atomic systems $\Delta\mu$ shows only a slight dependence on the degree of undercooling (expressed as $T^* = (T - T_M)/T$) via the entropy of freezing. For colloids the intrinsic energy scale may be significantly altered by adjusting the interaction potential. For a given sample $\Delta\mu$ has to be determined experimentally or via computer simulation. The nucleation barrier $\Delta G^* = 16\pi\gamma^3/3(\Delta\mu n)^2$. Here γ is the surface tension between melt and solid which for HSs should be on the order of $k_B T/a^2$.

Kinetic prefactors of atomic systems depend on temperature e.g. via a Maxwellian distribution of velocities. Additional modifications are necessary if an activated step is involved [34]. While temperature is the natural control parameter in atomic systems, colloidal systems crystallize quasi-isothermally. Here diffusive transport determines the kinetic prefactor. Growth is assumed to proceed via single particle attachment or—in the case of layering of the melt to the solid—by registering of adjacent planes. In both cases $v_\infty = Dd_I/l^2$, where D is an appropriate diffusion coefficient, d_I the thickness of the interfacial region and l the mean distance of fluid particles from their target place in the crystal. The prefactor in nucleation should be given by $J_0 = nD/l^2$, which approximating l by $n^{-1/3}$ leads to a $\Phi^{5/3}$ dependence.

Further in both kinds of system there is a competition between the time scale of equilibrating the control parameter throughout the system and its rate of change. This poses two fundamental difficulties. In nucleation during rapid quenches systems may not have time to evolve the control parameter dependent equilibrium distribution of fluctuations [32]. Experimental results thus may depend on the quench history. In addition, the transition itself may introduce local deviations from the initially adjusted global conditions. This concerns the release of latent heat in crystallization from the melt and the formation of depletion zones in crystallization from both solution and melt [35, 36]. As a consequence to growth instabilities like dendritic growth or secondary nucleation may result [37]. Owing to the presence of the suspending medium acting as an excellent heat sink colloidal crystallization proceeds quasi-isothermally. However, depletion zones and growth instabilities via density fluctuations are encountered, too.

A final important point is the accessibility by various approaches. Critical nuclei comprise some 10^2 to 10^4 particles and interfacial thicknesses about ten particle layers above the roughening transition. Thus the relevant length scales in both these cases are of the order of a few particle distances. This is no serious restriction to theoretical modelling and, in fact, a lot of progress has been achieved throughout recent years through e.g. the use of density functional methods [5, 6]. For experiments on atomic and molecular melts, however, it poses a formidable challenge. In addition, the short absolute time scales, the difficulties of controlling the temperature and the unavoidable presence of attractive interactions considerably complicate the situation.

Alternatively, computer simulations allow for variation of interaction potential, local control of temperature and microscopic modelling of events. In particular, growth was extensively studied for Lennard-Jones particles under stationary conditions and the WF growth law confirmed at moderate undercoolings [34]. In addition the interfacial structures could be determined for different crystallographic directions [38]. Isolated nucleation events are much more difficult to simulate due to the influence of the periodic boundary conditions [39, 40, 41]. In sufficiently large systems on the other hand nucleation is a rare event and special sampling techniques have to be employed to generate good statistics and/or to avoid the crystallization of the complete box from a single nucleus [42]. Besides estimates of nucleation rates also the nucleation path can be studied in quite some detail. For a system of spheres with an r^{-12} potential it was for instance observed that bcc nuclei form much more easily, as the nucleation barrier height is much smaller than for fcc even when fcc is the thermodynamically stable phase [43].

Colloid specific length scales are of the order of the wavelength of visible light and thus allow for access via microscopy and light scattering yielding complementary information from real and reciprocal space [7, 8, 44]. For Brownian dynamics the typical time for a non-interacting particle to diffuse the distance of its own radius a is in the millisecond range and may be calculated from the Stokes–Einstein diffusion coefficient $D_0 = k_B T/6\pi\eta a$, where η is the shear viscosity. Both direct interactions leading to structure formation [6, 10, 45]

and hydrodynamic interactions slow down the diffusive motion [25, 46], but in most cases the self-diffusion coefficients differ by only a few orders of magnitude in different phases. In combination with the low particle density of typically 10^{11}–10^{14} cm^{-3} (as compared to 10^{21} cm^{-3} in metals) this leads to a condensation of all relevant time scales for nucleation, growth and ripening to the narrow range of seconds to hours. Furthermore the solids may easily be shear molten e.g. by simply shaking the sample [47]. This is traced back to their extremely low shear modulus which is on the order of a few Pa only [48]. Whereas the energies of interaction are of the same order as in atomic systems (which results in thermally stable crystals) the low shear rigidity is caused by the low particle densities. Consequently metastable melts can be prepared from well characterized solids without gradients in the control parameters.

Colloidal suspensions thus have been recognized as versatile model systems for the study of phase transition kinetics and much progress has been reported over the last years. Yet these systems also introduce their own specific complications, like a distribution in particle size, a complex time and length scale dependence of transport processes, the very fragile nature of colloidal solids or the need to develop special techniques of sample preparation and investigation. In the next section we review the most important optical methods for the study of solidification kinetics.

3. Experimental techniques

A homogeneous colloidal melt can be prepared by application of random shear. Shortly after cessation of shear only short range order is present throughout the sample. If impurity nucleation is suppressed by filtering, nuclei may form by wall induced nucleation or by homogeneous nucleation in the bulk. By choosing a suitable cell geometry, each of these scenarios may be made dominant [49]. At the beginning of the homogeneous nucleation process a random distribution of denser crystals in pressure equilibrium with the adjacent melt may be assumed. Inter-crystal ordering may occur, once interactions between neighbouring nuclei are present. This may be caused by an approach of crystal surfaces (respectively depletion zones) during the late stages of solidification, by large nucleation rate densities or by an underlying spinodal type decomposition. The latter has not been systematically studied; however recent observations on very highly charged systems and on mixtures seem to support this possibility [50]. A further heterogeneity is observed concerning the orientation of crystals which again in most cases is random. The orientation correlation between crystals usually stays close to zero even if at late stages the position correlation increases. After complete solidification crystals are separated by grain boundaries, while in the coexistence region also bulk fluid remains. Further evolution of crystal shape and size is due to ripening and proceeds on comparably slow time scales.

Both light scattering and microscopy yield valuable information on the kinetics of solidification, as they may be adapted to the specific questions of interest. For example, growth is readily studied by microscopy, while nucleation kinetics have been investigated mainly by scattering techniques. In the following we outline both experiments as well as combined methods.

3.1. Scattering

The treatment of static and dynamic light scattering [51–53] is in many respects highly analogous to that of neutron or x-ray scattering [14, 54–56]. In our experiments we use an apparatus recording both Bragg scattering (BS) and small angle light scattering (SALS) [57].

We first treat polarized single scattering from long and short range ordered particles, and then consider SALS from density fluctuations, i.e. denser crystals as compared to the melt which itself may be of inhomogeneous density due to the formation of depletion zones.

We start by assuming the incoming beam to be a linearly polarized plane wave: $\boldsymbol{E}(\boldsymbol{r}) = \boldsymbol{E}_0 \exp(\mathrm{i}\boldsymbol{k}_i \cdot \boldsymbol{r})$, where the time dependence is omitted, since we consider elastic scattering only. The primary wave is incident on N spherical particles of radius a contained in the scattering volume V_S centred around $\boldsymbol{r}_0 = (0, 0, 0)$. We further assume a homogeneous distribution of particle number density $n = N/V_S$. Far from the sample the superimposed scattered fields may again be considered as a plane wave. The difference between incoming and scattered wave vector defines the scattering vector:

$$|\boldsymbol{q}| = |\boldsymbol{k}_0 - \boldsymbol{k}_S| = (4\pi \nu_S/\lambda_0) \sin(\Theta/2) \tag{3}$$

where Θ is the scattering angle as defined in figure 1, ν_S is the solvent refractive index and λ_0 the vacuum wavelength of the (laser) light. Restricting ourselves to single scattering events only, the scattered intensity is [52]:

$$I(\boldsymbol{q}) = C\,P(\boldsymbol{q})S(\boldsymbol{q}) \tag{4}$$

with the constant C:

$$C = \frac{V_S I_0}{R_D^2} \frac{\boldsymbol{k}_i^4}{(4\pi)^2} \frac{N}{V_S} (\boldsymbol{n}_0 - \boldsymbol{n}_S)^2 b(0)^2 \tag{5}$$

which comprises the geometry of the scattering experiment and the optical properties of the particle material. Here $I_0 = \frac{1}{2}(\varepsilon_s/\mu_0)^{1/2} E_0^2$ is the incident intensity, R_D is the distance between scattering volume V_S and the detector, $\boldsymbol{n}_0$ and $\boldsymbol{n}_S$ are the polarization vectors of incident and scattered light, respectively. The particle scattering amplitude at zero wave vector is given by the difference in refractive indices of particles and solvent times the particle volume: $b(0) = (\nu_P - \nu_S)(4/3)\pi a^3$. The particle form factor $P(\boldsymbol{q}) = b(\boldsymbol{q})^2/b(0)^2$ is normalized by $b(0)^2$ to result in $P(0) = 1$. It describes the angle dependence of single particle scattering. To be specific, for small polystyrene spheres ($\nu_P = 1.590$) of $a < 60$ nm in water ($\nu_S = 1.333$) it often is sufficient to use the Rayleigh–Debye–Gans approximation for small q data:

$$b(q) = \frac{4\pi(\nu_P - \nu_S)}{q^3} (\sin(qa) - qa\cos(qa)). \tag{6}$$

Polydispersity, bimodal mixtures, deviations from spherical shape and the corresponding influence of particle orientation may be treated within extensions of this approximation [46]. For larger particles and those with radial variations in ν_P Mie scattering theory applies.

$S(\boldsymbol{q})$ contains all the information about the particle positions $\boldsymbol{r}_i$. It is defined as:

$$S(\boldsymbol{q}) \equiv \frac{1}{N} \sum_{i=1}^{N} \sum_{j=1}^{N} \langle \exp(\mathrm{i}\boldsymbol{q} \cdot (\boldsymbol{r}_i - \boldsymbol{r}_j)) \rangle \tag{7}$$

where the brackets $\langle \ldots \rangle$ denote the ensemble average. $S(\boldsymbol{q})$ differs for differently structured phases. Throughout solidification crystallites coexist with remaining fluid. If particle positions in different phases are uncorrelated, in reciprocal space an incoherent superposition of melt and crystal scattering is observable.

In the isotropic melt colloidal particles possess short range order only. The particle positions are usually represented as the conditional probability to find a second particle at a distance r, if a first particle is at the origin. This radial distribution function $g(r)$ may be taken from computer simulations or calculated from integral equations of Ornstein–Zernicke type

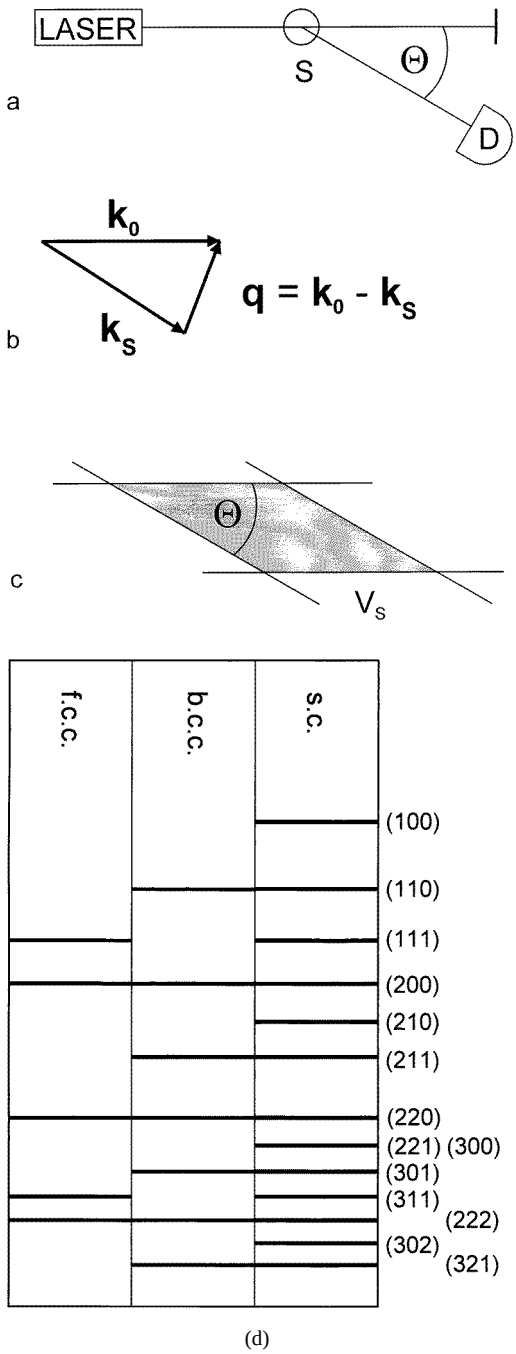

Figure 1. (a) Scheme of a light scattering experiment. S: sample; D: detector; Θ: scattering angle. (b) Scattering vector. (c) Scattering volume. (d) Scheme of Bragg reflections for different crystal structures.

with appropriate closures [46]. The scattering probability depends only on the modulus of $\boldsymbol{q}$

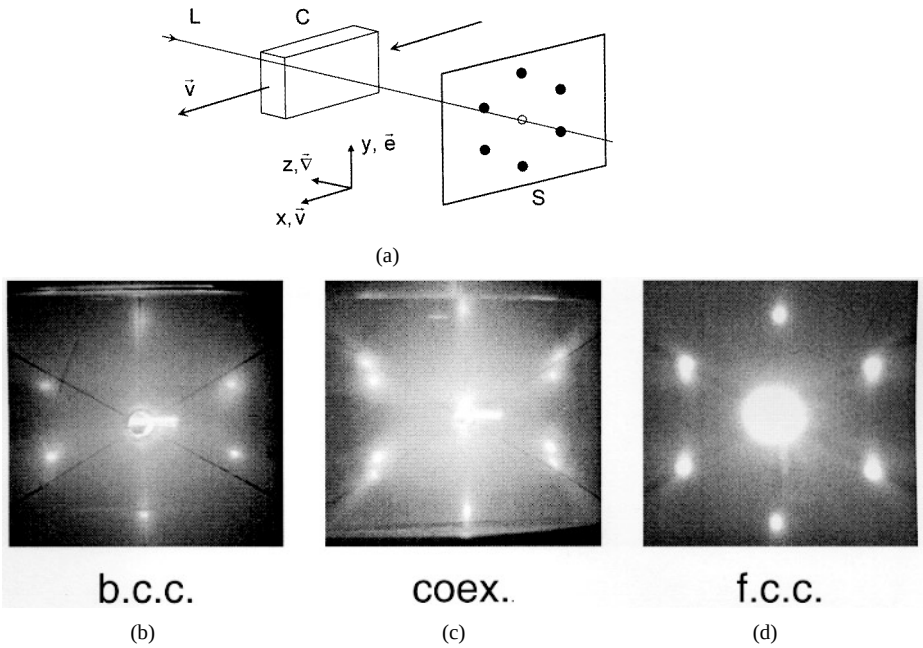

Figure 2. (a) Recording of two dimensional scattering pattern from single crystals. L: laser beam; C: sample cell; S translucent screen; the coordinate system identifies flow direction $\boldsymbol{v}$, gradient direction $\boldsymbol{\nabla}$ and vorticity direction $\boldsymbol{e}$. Scattering patterns taken for PS120 at (b) $n = 2.5\times10^{18}$ m^{-3} (c) $n = 3.7 \times 10^{18}$ m^{-3} (d) $n = 6 \times 10^{18}$ m^{-3}. Lines intersecting at 60° are guides to the eye [48].

and the melt or fluid structure factor is written as [52]:

$$S_F(q) = 1 + n\int_{V_S} \mathrm{d}\boldsymbol{r}\, g(r)\exp(\mathrm{i}\boldsymbol{q}\cdot\boldsymbol{r}) = 1 + n\int_{V_S} \mathrm{d}\boldsymbol{r}(g(r)-1)\exp(\mathrm{i}\boldsymbol{q}\cdot\boldsymbol{r}) + n\int_{V_S} \mathrm{d}\boldsymbol{r}\exp(\mathrm{i}\boldsymbol{q}\cdot\boldsymbol{r}). \tag{8}$$

The first integral is independent of the scattering volume and is conventionally identified with the static structure factor $S_F(q)$ measured at $q \neq 0$. In the limit of $q \to 0$ it is connected to the isothermal compressibility. It shows pronounced oscillations for $q \geqslant d_{NN}$, where $d_{NN} = n^{-1/3}$ is the average nearest neighbour distance, and approaches 1 for $q \to \infty$. The second term contains information about V_S and for $V_S = \infty$ contributes a delta function at the origin: $S(0) = nV_S = N$. For small V_S this peak will be broadened according to the size and shape of V_S. $S_F(q > 0)$ is not altered as long as the size of V_S is larger than the order correlation length in the melt.

For long ranged crystalline order the distribution of particles $\rho(\boldsymbol{r})$ is a periodic function. In reciprocal space this corresponds to a set of lattice vectors $\boldsymbol{g}_{hkl} = h\boldsymbol{b}_1 + k\boldsymbol{b}_2 + l\boldsymbol{b}_3$ forming the reciprocal lattice (where h, k, l are the Miller indices). From the squared modulus of the Fourier transform of $\rho(\boldsymbol{r})$ an ideal crystalline structure factor $S_C^0(\boldsymbol{q})$ may be derived. For the infinite crystal this is a set of delta functions. Intensity is observed whenever $\boldsymbol{q} = \boldsymbol{g}_{hkl}$, i.e. when the Ewald sphere intersects with $S_C^0(\boldsymbol{q})$. For lattices with more than one lattice point per unit cell (like bcc or fcc) selection rules determine the h, k, l for which scattering is observed (cf figure 1(d)).

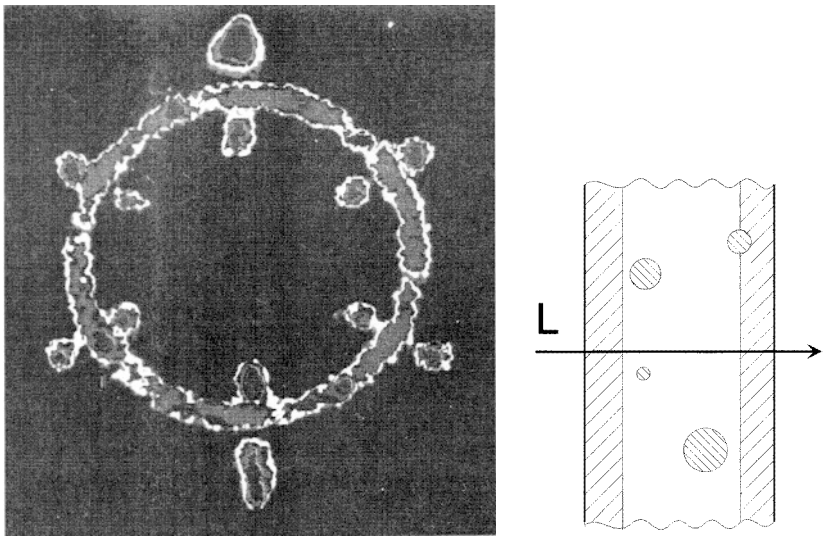

(a) (b)

Figure 3. (a) Scattering pattern recorded in a thick cell during solidification of PS109. (b) Sketch of the corresponding situation in real space. L: laser beam; shaded region: crystalline phase.

Single crystals may be grown via heterogeneous wall nucleation. To identify their structure and orientation the symmetry of two dimensional scattering patterns may be exploited, e.g. using the simple set-up sketched in figure 2(a). The intensity distribution is observed on a translucent screen by a CCD camera to result in video frames as given in figure 2(b)–(d) taken across the bcc/fcc phase transition after complete solidification. Twinned fcc and bcc structures are identified which are oriented with their densest packed planes $\langle 111 \rangle$ and (110) perpendicular to the laser beam. The direction of easiest shear within these planes $\langle 111 \rangle$ is oriented parallel to the formerly applied shear flow direction. Additional information on the real space distribution of scatterers is obtained, if no focusing optics are used at all. Figure 3(a) shows the scattering pattern recorded during solidification in a thick cell corresponding to the situation schematically drawn in figure 3(b). Here, the ring pattern originates from the fluid phase; the six doublets are generated by the two growing wall crystals on the cell front and rear. A similar thick cell set-up has been used to determine the spatial distribution of phases in solidification under flow [58].

Focusing optics facilitate the recording of time dependent intensities at exactly defined $\boldsymbol{q}$. In the case of wall crystal growth the peak intensity contains a lot of additional information. This is seen from figure 4, where the reflected and transmitted intensity are recorded for a bcc crystal like the one shown in figure 9(a). The illuminated spot covers a number of initially columnar twins (cf figure 9(b)) but intensity is recorded for only one of the six (110) directions. The initial increase of the peak intensity $I(q_M, t)$ is quadratic and linear growth velocities for very early stages can be extracted. At later times stacking faults interchange the twin species leading to a deviation from the quadratic increase. This artefact is thus not present if the sum over all six peak intensities is recorded. Further, fast oscillations are present which result from thermally excited shear waves in the wall crystals [59]. Knowing the corresponding crystal thickness, the shear modulus can be obtained. Slow oscillations at medium times originate from interference effects between front and rear crystals, while irregular late stage fluctuations stem from straining during the ripening of the twin domains.

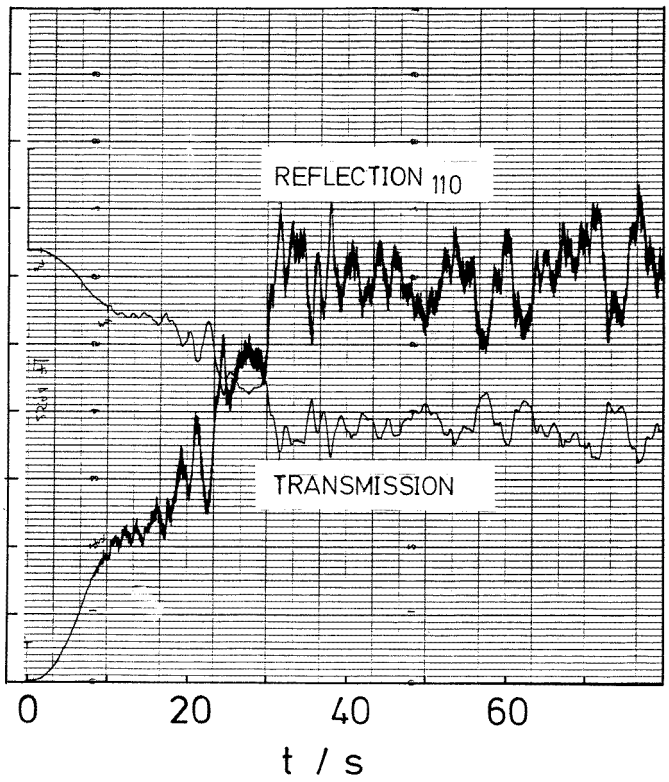

Figure 4. Diffracted and transmitted intensity for a PS109 sample crystallizing in a thick cell. Intensity was recorded for one of the six (110) reflections only.

Experimentally, a considerable broadening of peaks is often observed. In turbid samples it may be caused by multiple scattering [48] not considered here. In transparent samples and in particular for fine grained polycrystalline solids or growing crystals embedded in the melt also finite size broadening occurs and intensity is present at $\boldsymbol{q} \neq \boldsymbol{g}_{hkl}$. The order correlation length now is restricted to the crystal size. For quantitative calculation the real space particle distribution $\rho(\boldsymbol{r})$ is multiplied with a function describing the size and shape of the crystal under consideration. The Fourier transform of this product yields a convolution of the Fourier transforms of particle distribution and shape function. Since the convolution applies to the delta functions only we write for the resulting structure factor:

$$S_C(\boldsymbol{q}) = S_C^0(\boldsymbol{q}) \otimes H_C(\boldsymbol{q}) \tag{9}$$

where $\boldsymbol{q} \neq 0$. The zero q peak again shows broadening due to the finite size of the sample and becomes important if a single crystallite fills V_S. A nice two dimensional illustration of this case can be found in the book by Born and Wolf [56].

The next step is to find adequate expressions for the shape function and the crystal shape factor $H_C(\boldsymbol{q})$. We consider a crystal shaped as parallelepiped with axis lengths $L_j = N_j|\boldsymbol{a}_j|$ with $j = 1, 2, 3$, and N_j as the number of lattice planes in the direction of the basis vector $\boldsymbol{a}_j$. We further assume an orthogonal unit cell, where the $\boldsymbol{a}_j$ are parallel to the $\boldsymbol{b}_j$. Then a set of

Heaviside functions may be chosen for $H(\boldsymbol{r})$. The corresponding shape factor is:

$$H_C(\boldsymbol{q}) = \frac{\sin^2(\pi \boldsymbol{q}_1 L_1)}{\pi \boldsymbol{q}_1^2 a_1^2} \frac{\sin^2(\pi \boldsymbol{q}_2 L_2)}{\pi \boldsymbol{q}_2^2 a_2^2} \frac{\sin^2(\pi \boldsymbol{q}_3 L_3)}{\pi \boldsymbol{q}_3^2 a_3^2}. \tag{10}$$

For each direction, at the peak ($\boldsymbol{q} = \boldsymbol{q}_m = \boldsymbol{g}_{hkl}$) the intensity will be proportional to the square of the number of lattice planes N_j^2 while in the tails the intensity oscillates and decreases as $\boldsymbol{q}_j^{-2}$. The integrated intensity along each direction will be proportional to N_j/a_j, and the full width at half height proportional to $1/N_j a_j$. Thus parallel to a direction where the crystal is thin the distribution of scattered intensity is broad: a platelike crystal, for instance, will give rise to a rodlike structure of the peaks, and *vice versa* [35, 56].

If more than one crystal (phase) is present their scattering patterns superimpose incoherently. The resulting total structure factor $S(\boldsymbol{q})$ is:

$$S(\boldsymbol{q}) = \frac{N_F}{N} S_F(q) + \sum_i \frac{N_{C,i}}{N} S_{C,i}(\boldsymbol{q}). \tag{11}$$

$N_{C,i}$ and N_F are the number of particles in each crystallite i and in the fluid phase, respectively. Note that still a homogeneous density is assumed throughout the whole sample.

These considerations have been used in numerous experiments. Strongly anisotropic $H_C(\boldsymbol{q})$ are, for instance, useful in analysing the stacking probability of hexagonal (111) lattice planes in HS crystals and its temporal development. While a stacking sequence of ABAB corresponds to a hexagonal close packed (hcp) structure and ABCABC to an fcc crystal, random stacking may occur during rapid growth. If growth is slower still stacking faults may be present leading to a pancake-like stacking of thin slices e.g. of fcc crystal. Both lead to Bragg rods rather than Bragg spots in reciprocal space. As in atomic systems the width of these may be determined, if a single crystal specimen is rotated about specific axes perpendicular to the incoming beam. Otherwise orientational averaging has to be performed leading to a characteristic anisotropic broadening of the (111) peak [10, 60]. Thick slices are observable also in polarization microscopy [61] and also occur in oriented monolithic crystals. Dux and Versmold measured their annealing kinetics through a careful analysis of the time dependence of peak widths and found an exponential decay of the number of stacking faults [62]. In time averaged neutron scattering data of samples under shear information about the sliding of stacks and single planes is obtained [63, 64].

During early stages of growth structurally homogeneous spherical crystallites of radius R prevail. After solidification facets appear along the contact lines of crystals. The resulting mosaic is still conveniently represented by a set of spherical (or cubic) crystals of average radius (side lengths). Their scattering patterns superimpose. To calculate the scattering pattern for large numbers of randomly orientated crystals an orientation average has to be performed. In particular, for a powder of spherical crystallites $H_C(q)$ can be derived from the Rayleigh–Debye–Gans approximation and the intensity $I(q-q_m)$ can be calculated performing a double integration over q to yield [65]:

$$I(q-q_m) \propto \frac{1}{2R^4(q-q_m)^4}(1-\cos(2(q-q_m)R) - 2(q-q_m)R\sin(2(q-q_m)R) + 2(q-q_m)^2R^2). \tag{12}$$

Usual Debye–Scherrer experiments have a fixed detector and a rotating sample (cf figure 1(a)). Our apparatus for simultaneous detection of Bragg and small angle powder scattering is shown in figure 6(a). There, to avoid mechanical disturbances, the sample is fixed and the Bragg detector which is an array of photodiodes mounted on an arm is rotated around the optical axis. Thus either the full two dimensional scattering pattern [66], or after angular averaging

the usual Debye–Scherrer pattern, is recorded [57]. From the sequence of Bragg peaks the crystal structure can be inferred. A similar construction is used for the small angle regime where a ring pattern is observed to grow in time. An example of the BS pattern observed for a bcc CS solid (seventh peak present) is given in figure 5 [67]. An example of time resolved BS and SALS measurements during solidification of a HS system is given in figures 6(b) and (c), respectively.

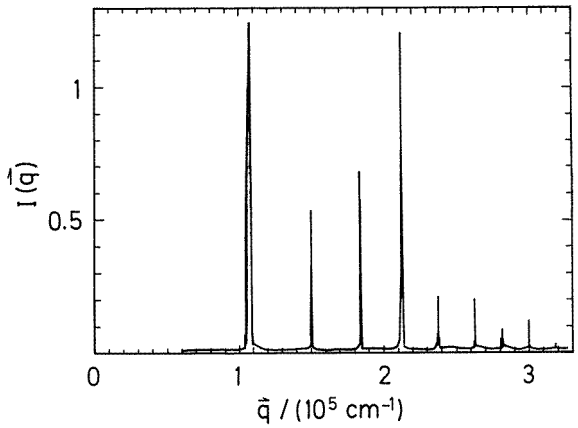

Figure 5. Debye–Scherrer pattern for PS91 at $n = 3.4 \times 10^{18}$ m^{-3}.

$S_C(q)$ is obtained from the raw BS pattern after dividing out the particle form factor $P(q)$ (either calculated or measured on a dilute sample) and subtracting the fluid structure factor (as known from an early measurement). Figure 7 gives an example for this procedure taken from Harland and van Megen [68] for the (111) reflection. If the form factor is not known, one may divide by an early measurement only [66], thus correcting for $P(q)$ but introducing an ill defined background variation in the region of the oscillations in $S_F(q)$. Then only those peaks in $S_C(q)$ are accessible for further evaluation which show a sufficiently small background variation to allow for a simple subtraction procedure. For the measurements shown in figure 6(b) this will be possible for (220) and (311).

From the knowledge of $S_C(q)$, the full width at half height $\Delta q_{1/2}(t)$ and the position of the maxima $q_M(t)$ the following kinetic quantities are obtained [68]. Firstly the fraction of crystalline phase $X(t)$ is obtained as an integral over the reflection (hkl):

$$X(t) = cI_{hkl} = c\int_{q1}^{q2} S_C(q)\,\mathrm{d}q \tag{13}$$

where for $\Phi > \Phi_M$ the normalization constant c is chosen such that $X(t \to \infty) = 1$. Typical q_1, q_2 are indicated in figure 7.

Secondly, the average linear dimension L is accessible through:

$$L(t) = \pi K/\Delta q_{1/2}(t)\,a \tag{14}$$

where K is the Scherrer constant for a cube shaped crystal. For the (111) reflection $K = 1.155$ [69]. For spherical crystallites $R(t)$ is determined from a fit of equation (12). Finally, the number density n_C of average sized crystals may be inferred from:

$$n_C(t) = X(t)/L^3(t) \tag{15}$$

and the nucleation rate density as $J = (\mathrm{d}n_C/\mathrm{d}t)/V_S$. Several authors approximated the time dependencies of the crystallized volume by power laws: $V_C \propto t^\alpha$. For constant J,

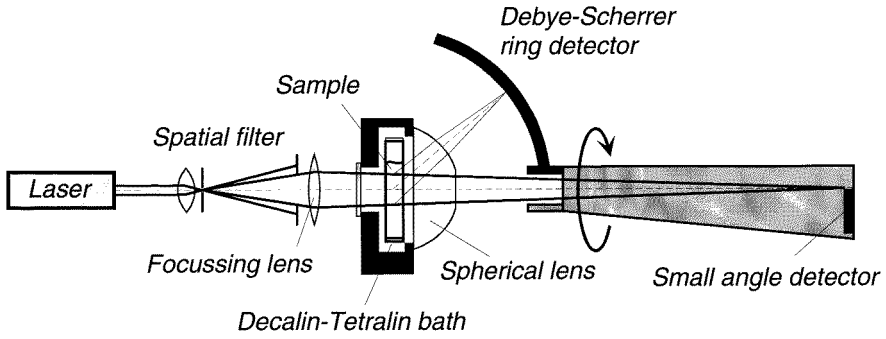

(a)

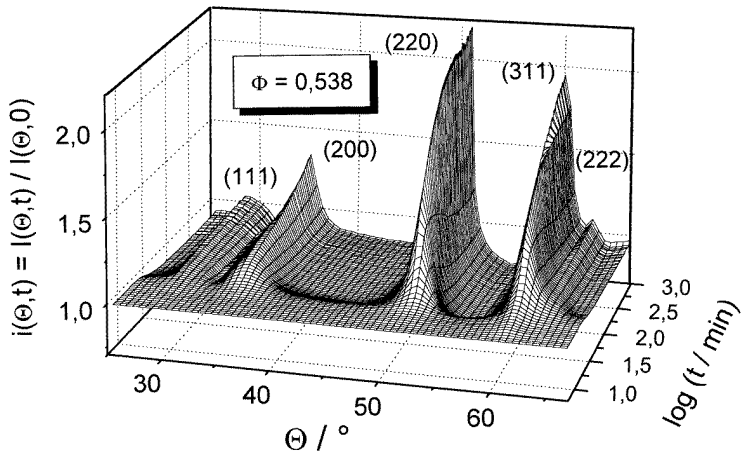

(b)

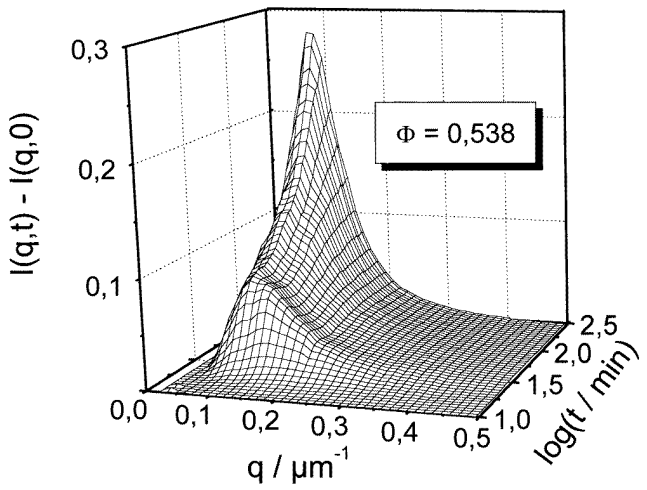

(c)

Figure 6. (a) Apparatus for simultaneous recording of BS and SALS; (b) time resolved BS experiment; (c) time resolved SALS experiment; PMMA890, $\Phi = 0.538$. Data are plotted versus the scattering angle Θ. For our wavelength of $\lambda = 632.8$ nm the corresponding q-range is (6–15) $\mu\mathrm{m}^{-1}$.

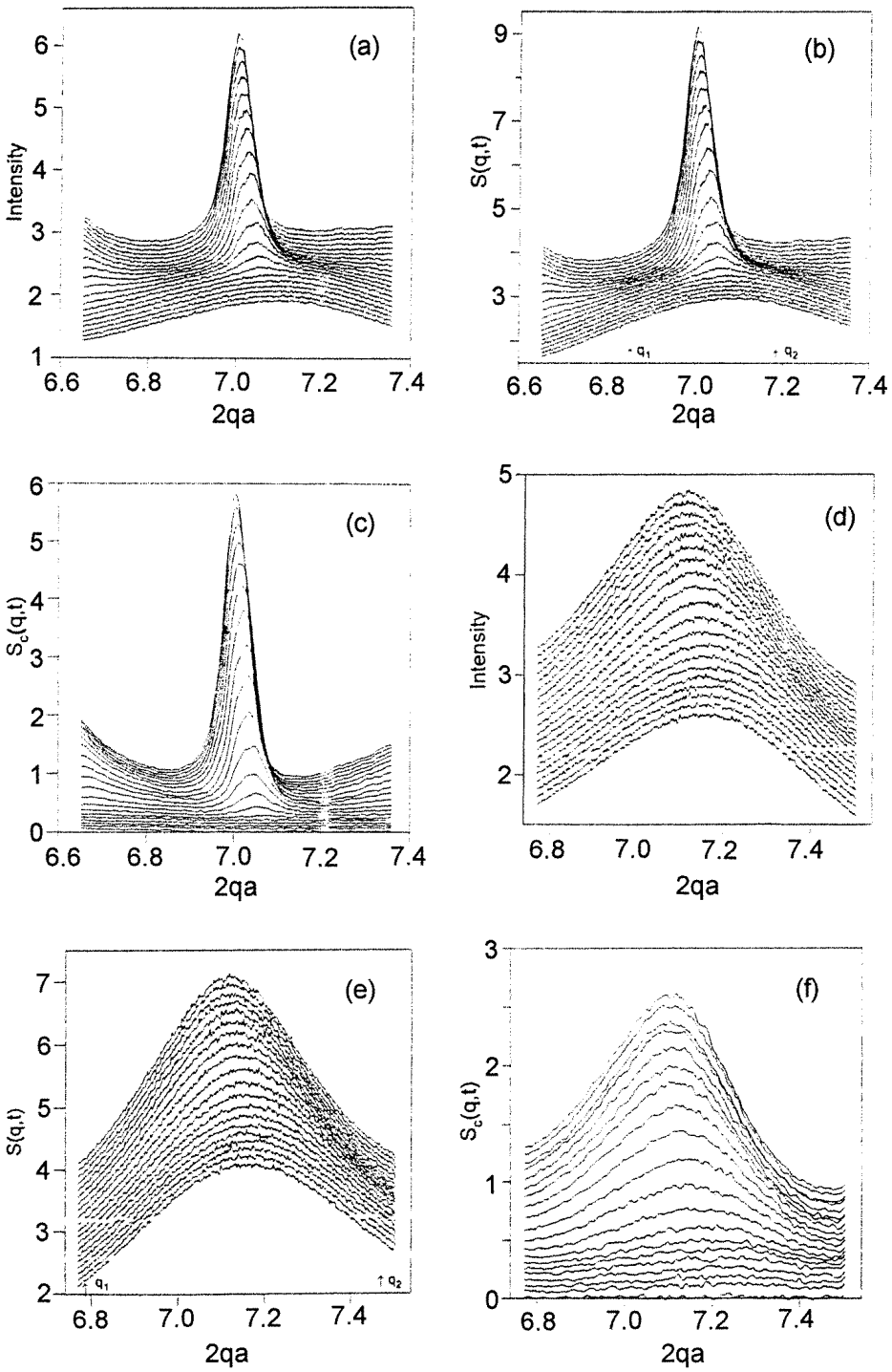

Figure 7. Extraction of crystal static structure factors $S_C(q,t)$ from raw intensities $I(q,t)$. Upper row: PMMA402 $\Phi = 0.537$; lower row: PMMA402, $\Phi = 0.557$. Left: $I(q,t)$; middle: $I(q,t)/P(q)$; right: $S_C(q,t) = S(q,t) - S_F(q,t)$. Curves are shifted for clarity. With kind permission from [68].

$\alpha_{NUCL} = 1$, for reaction limited growth $\alpha_{GROWTH} = 3$ and for diffusion limited growth $\alpha_{GROWTH} = 2/3$. In a simplified model $\alpha = \alpha_{NUCL} + \alpha_{GROWTH}$ are compiled in table 1. While the individual crystallite continues growing with constant α_{GROWTH} the average also contains freshly nucleated crystals. More sophisticated approaches therefore account for the reduced average growth exponent caused by continued nucleation as well as the reduction of free volume available for nucleation during solidification (see e.g. the paper of Aastuen *et al* in [7]).

Table 1. Expected exponents for the temporal evolution of integrated intensities I, peak positions q and peak widths Δq during crystallization.

Growth exponent t^{α}	Growth reaction limited $R \propto t^1$	Growth diffusion limited $R \propto t^{1/2}$
I_{BS}	4	5/2
$\Delta q_{1/2,BS}$	−1	−1/2
I_{SALS}	7	4
$q_{m,SALS}$	−1	−1/2

Thus far we have considered samples with no density difference between melt and crystal. This assumption is not strictly fulfilled in experimental situations. In the coexistence region of the phase diagram the equilibrium phases differ by some 10% in density. Also above melting crystals may be transiently compressed as has been shown by following the temporal evolution of lattice spacings $d_{hkl}(t) = 2\pi/q_m(t)$ [68]. Further particles may be attached faster to the crystal surface than they are transported to the interface from the melt bulk. This results in the formation of depletion zones around the crystallite. In each case additional scattering at low q arises from such long range (as compared to particle spacings) density fluctuations. Note that this does not affect the broadening of Bragg peaks as long as the crystal phase remains homogeneous. For large depletion zones, however, $S_F(q)$ may be affected.

To be specific SALS ring patterns arise either from the long range variation in mean refractive indices stemming from the particle number density variation of crystal plus depletion zone or from a short range ordered array (rather mono-disperse) crystals. The mean refractive index of a crystal is $\nu_C = \Phi_C \nu_P + (1 - \Phi_C)\nu_S$, where the subscripts P and S denote particle and solvent, respectively. The mean refractive index of the melt ν_F is calculated accordingly. A zero q scattering amplitude is defined analogous to the single particle case: $b^*(0) = V_C(\nu_C - \nu_F)$, where V_C is the volume of a crystallite. The crystal form factor is given by $P^*(\boldsymbol{q}) = b^*(\boldsymbol{q})^2/b^*(0)^2$. Assuming a spherical shape with sharp boundaries an analogue of equation (6) may be used for $b^*(q)^2$. The initial distribution of crystallites is random; inter-crystallite ordering may evolve at late stages, e.g. due to crystals competing for particles and may be described using an inter-crystallite structure factor $S^*(\boldsymbol{q})$. Assuming the typical dimensions of crystalline and fluid regions to be large as compared to d_{NN} but small as compared to $V_S^{1/3}$ and the isothermal compressibility to be very low, the contributions of $S_F(q)$ and $S_C(\boldsymbol{q})$ at $q > 0$ may be neglected. The time dependent SALS intensity then is:

$$I(\boldsymbol{q}, t) = C P^*(\boldsymbol{q}, t) S^*(\boldsymbol{q}, t). \tag{16}$$

Averages over many crystallites again result in $I(q)$. They contain a large amount of information and often are not easy to interpret. $P^*(q)$ may appear broadened by the size distribution resulting from continued nucleation. Further, model assumptions about the density profile as a function of time are required, which may have a rather complex form. At later stages inter-crystallite ordering may destroy spherical symmetry and lead to deviations of $S^*(q)$ from one.

Time resolved SALS experiments on crystallizing HSs show a pronounced ringlike scattering pattern [70] well known from spinodal decomposition but also from crystallization experiments on atomic melts [36]. Rather than using $I(0)$, here $I(q)$ is normalized by $I(q_m)$. Furukawa [71] suggested a simple model function for cases where fluctuations in the conserved order parameter particle density give rise to a peak at q_m in SALS:

$$\frac{I(q,t)}{I(q_m,t)} = \frac{3Q(t)^2}{2+Q(t)^6} \tag{17a}$$

with $Q = q/q_m$. The scaling corresponds to a constant shape of the growing object. This may also apply to HS crystal growth and Schätzel and Ackerson [70] therefore suggested to check SALS data for scaling laws using the following empirical formula:

$$\frac{I(q,t)}{I(q_m,t)} = \frac{27Q(t)^2}{(2+Q(t)^2)^3} \tag{17b}$$

where $I(q)/I(q_m)$ actually corresponds to the shape of the total object but in the literature often is referred to as the crystal form factor. The position of the maximum is inversely proportional to the radius of the scattering object, $q_m \propto 1/R$, and the peak intensity is proportional to the square of the object volume, $I(q_m) \propto V_2 \propto R^6$. While in near critical spinodal decomposition experiments, where there is the same length scale for both depleted and enriched phase, Furukawa scaling is nearly always observed, in HS crystallization only punctuated scaling obtains [72]. This is caused by the change of the relative size of the depletion zone as compared to the crystal, which in turn is mainly due to the beginning overlap of depletion zones at intermediate stages. It also originates from the competition of individual crystallites for particles. In short, a complex dependency of the growth velocity results which is observed as long lived transients for the growth exponents, say of the overall scattered intensity or q_m [73, 74]. Generally a slower than expected initial growth is observed, but also a maximum of growth velocities may occur. The form of the small angle peak is much less affected [75].

We focus on an evaluation for growth velocities and nucleation rates. For the broad peaks observed at early stages the evaluation of $q_{1/2}(t)$, the scattering vector at which $I(q,t)I(q_m,t) = 1/2$, yields a more stable size estimate than q_m. We use an empirical four parameter fitting function additionally accounting for a finite sized depletion zone through a variable width parameter C and the large q decay with an exponent $-\delta$, which may show deviations from the expected value of 4 as the depletion zones start overlapping. Details are given elsewhere [65, 76]. To obtain absolute crystallite sizes the fitting formula is set equal to the form factor of a solid sphere for $q > q_m$ and solved for the crystal radius to yield [65, 76]:

$$R(t) = \frac{1.8148}{q_{1/2}(t)}. \tag{18}$$

Figure 8 compares the absolute values for $R(t)$ from BS and SALS to show quite a good agreement in the growth law. SALS radii are somewhat larger, though. Note in both experiments crystals appear to be some 5 μm at $t_I = 15$ min.

3.2. Microscopy and combination methods

Light microscopy is a very versatile tool [12], as for sufficiently large particles it may directly reveal the spatial ordering [77] in the sample but on the other hand at lesser magnification shows the sample morphology [78]. In principle all conventional techniques may be employed like interference and phase contrast [79], confocal illumination [80] or polarization microscopy [61]. Interestingly, for sufficiently small numbers of individual crystallites in the light path, also

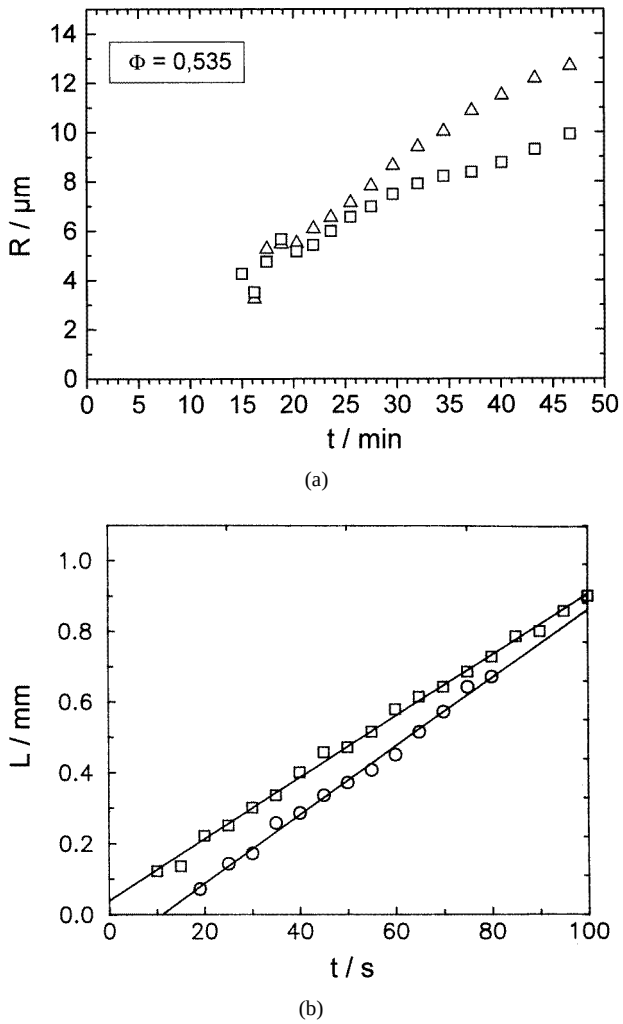

Figure 8. (a) Comparison of crystallite radii as a function of time from SALS (△) and BS (□). PMMA890, $\Phi = 0.535$. (b) Comparison of crystallite radii (○) to wall crystal thickness (□) for PS109*.

crystals of cubic structure give rise to coloured patterns if observed between crossed polarizers. This is not due to optical anisotropy but rather depends on the change in polarization of the scattered light and is described by dynamic diffraction theory [81]. This can be employed to study the stacking fault structure of fcc crystals [82], new growth instabilities [61] or the reduction of nucleation rates under shear [49].

A particularly nice technique was employed by some authors which relies on the combination of scattering and microscopy which henceforth will be called Bragg microscopy (BM). In their pioneering study on nucleation and growth, Aastuen *et al* observed the sample by a video camera equipped with a macro-lens [83]. Occasionally a crystallite was orientated such that its Bragg reflection was directly collected by the camera. Since the objective covered a finite q-range of $\Delta q > 2\pi/L$, the image of the crystal is reconstructed from the diffracted light allowing for an analysis of its growth velocity. Detailed studies on this technique with

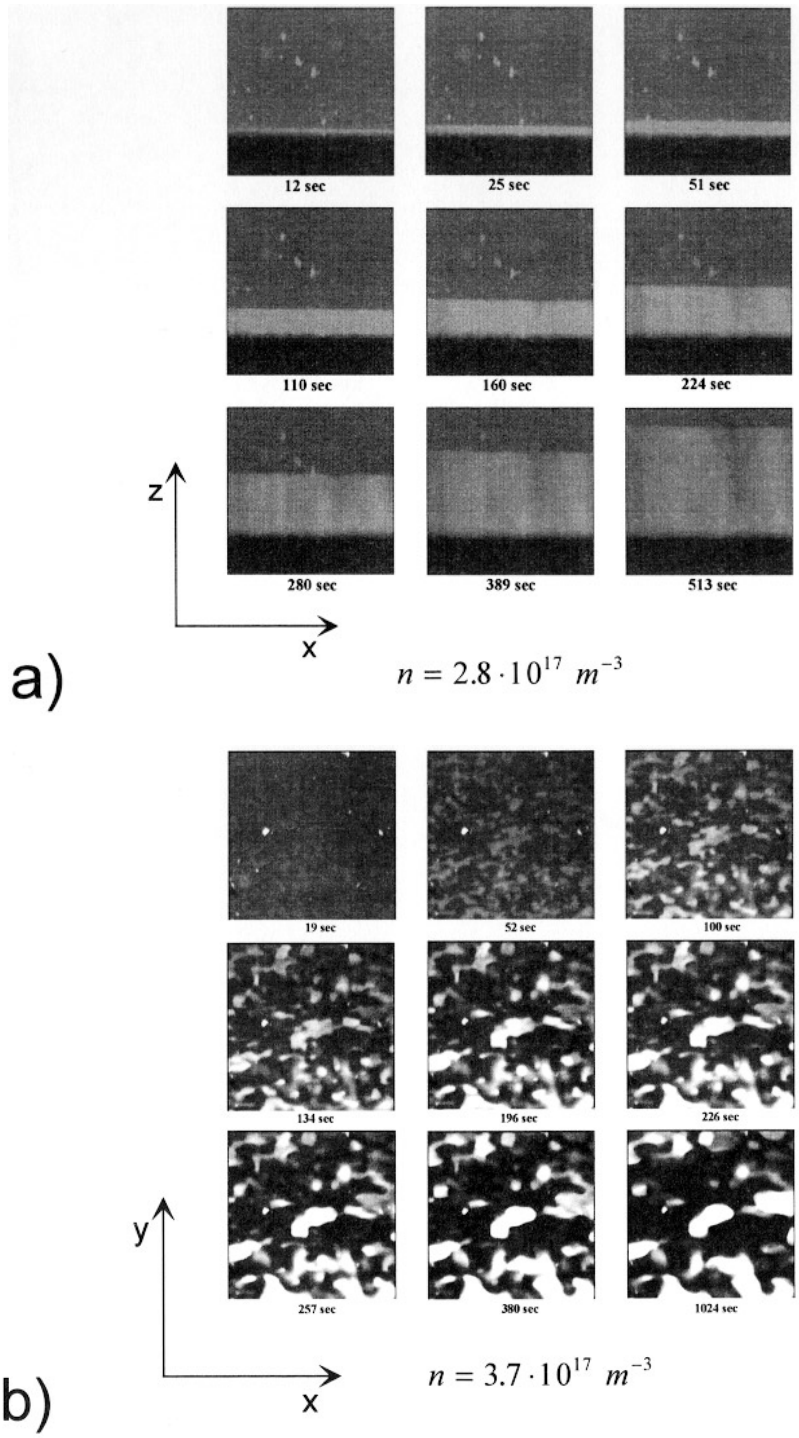

Figure 9. Bragg micrographs taken at different times as indicated. (a) Growth in z-direction: the shown area corresponds to $3.2 \times 2.4\ \text{mm}^2$; the light region is the wall crystal. (b) Development of bcc twin domains in the x–y-plane.

abundant examples for unusual and regular morphologies have been given by Okubo [84]. If the detector is placed off peak crystals appear as dark regions within a moderately scattering melt. Such crystals have been termed 'ghosts' [85]. Two examples of Bragg micrographs of wall crystals growing against the melt and of the ripening of bcc twin domains are given in figure 9 [86]. In the latter case contrast between domains is provided by the different scattering pattern orientation; one twin appears as ghost. For the sample in figure 9(b) the contrast increases as the crystal thickness in the z-direction increases. Three shades of grey are observed as scattering regions are situated both on the top and bottom sides of the cell.

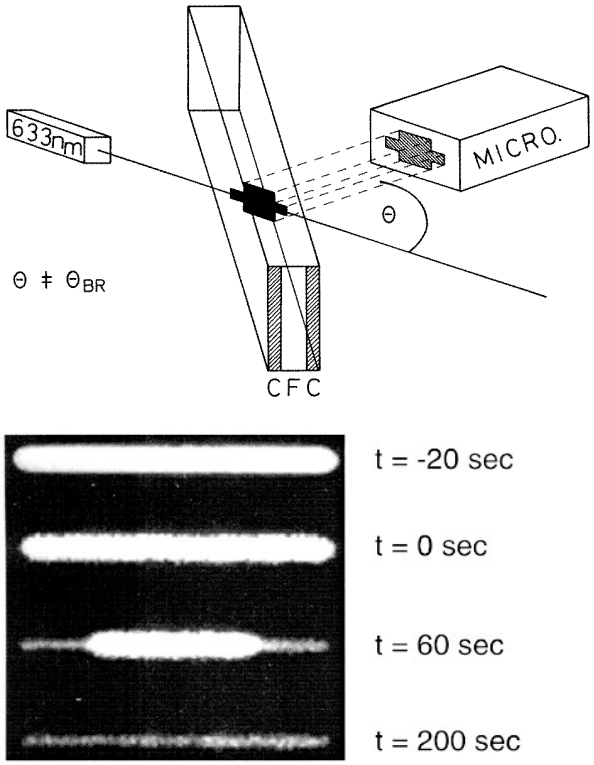

Figure 10. (a) Set-up for laser Bragg microscopy. C: wall crystal; F: fluid. (b) Bragg micrographs taken on growing crystals after layering induced heterogeneous nucleation at the cell wall. Time progresses from top to bottom, $t = 0$ is defined by abortion of shear flow. Bright: melt phase; grey: crystal phase.

To avoid multiple pictures when illuminating with white light coloured filters may be used, otherwise illumination can be done with a laser beam. To avoid the appearance of too many crystals on the video frame a slit or ultramicroscopic illumination should be used. This has for instance been employed in our studies on the structure of flowing systems [87] and on the growth velocity of wall nucleated crystals. A CCD camera observes the image of the laser beam crossing the cell at an angle to the optical axes (figure 10(a)) [88]. If the camera is placed in a direction where $S_F(\boldsymbol{q}) \gg S_C(\boldsymbol{q})$ the bright zone in the middle of the video frames represents the remaining melt, while the comparably dark zones are the two growing crystals (figure 10(b)). As the cell depth is fixed, large angles of incidence may be chosen to enhance the spatial resolution. Image processing then gives the crystal thicknesses L as a function of time as is shown in figure 8(b) comparing the case of homogeneously nucleated ghosts and

the case of wall nucleated crystals. Both spatial and temporal resolution of this technique are less good than for scattering; growth velocities obtained from fits to recorded crystal thickness are, however, accurate in the 10^{-2} μm s^{-1} range.

4. Solidification of hard sphere suspensions

4.1. Preparation and expected phase behaviour

Considerable progress was reported on HS suspensions, both due to the further development of scattering techniques and the availability of new, well characterized model systems. Several experimental realizations of HS systems have been reported: PMMA (polymethylmethacrylate) spheres coated with stabilizing PHSA (polyhydroxystearic acid) [25, 89], PS (polystyrene) [90] or PMMA [85] micro-network particles. Interesting new developments comprise core–shell particles or thermosensitive gels showing a temperature dependent packing fraction at constant particle density [91]. Often a near perfect index match is obtained using organic suspending liquids. Experimental systems closely follow theoretical predictions for HS also concerning dynamic quantities like diffusion and viscosity.

For HSs the only relevant parameter is the packing fraction Φ. It is calibrated against the phase behaviour most conveniently by the sedimentation method of Paulin *et al* [92]. The phase behaviour of monodisperse samples [24, 25] follows the theoretical predictions [21] based on the semi-empirical Carnahan–Starling equation of state [93] for the melt and results from computer simulations for the crystalline phase [94]: independent of particle size freezing occurs at $\Phi_F = 0.495$ and melting at $\Phi_M = 0.545$; for comparison: random close packing is at $\Phi = 0.64$ and the maximum value for one component systems is $\Phi = 0.74$ achieved for fcc and hcp. A kinetic glass transition is reported to occur under normal gravity at $\Phi_G = 0.57$ close to loose random packing [25]. Recent theoretical work further indicates that polydispersity will broaden the coexistence regime and shift it towards larger Φ values [95]. It is not clear, yet, whether this will be accompanied by a size segregation [96]. In any case crystallization should be suppressed above a critical polydispersity which has been estimated to be of the order of some ten per cent. Simulations show an HS crystal to wet a smooth hard wall with its (111) lattice plane enabling homo-epitaxial growth of partially oriented crystals [97]. This may not apply to restricted geometries where a number of quite exotic packings have been observed [12, 98]. Free energy differences between fcc and hcp structures as derived from theory and simulation are very small [99]. While absolute values are in fact still under discussion recent computer simulations favour fcc [100, 101]. In experiments these small differences of energies, respectively entropies, result in the occurrence of stacking faults [10, 61]. In annealing experiments on strongly screened CSs [62] and our own studies on PMMA particles a clear preference for fcc is observed.

4.2. Morphologies

Despite the principal simplicity of the problem there is a surprising richness in possible growth scenarios. Most crystal surfaces observed in purely repulsive systems were rough, leading to roundish morphologies during growth. In the coexistence regime of CSs dendritic instabilities may evolve, or growth may proceed from isolated islands forming hemispherical caps of crystallites [61, 82]. Dendritic growth also is observed for homogeneously nucleated HS crystals with surrounding depletion zone under various conditions [85] and has been treated in terms of linear stability analysis. In fact, there are indications that irrespective of volume fraction this is a normal growth mode under conditions of μ-gravity [74], where the dendrites are not sheared off the growing crystallite. It is not present in fluidized beds [9] or time

averaged zero gravity [102].

The conceptually most appealing situation of heterogeneous, layering induced nucleation with plane crystal–melt interfaces is difficult to prepare and has as yet not been studied systematically. Columnar growth, however, is observed for settling suspensions [103] with (111) parallel to the sample cell bottom. At low settling rate nearly defect free single crystals may be grown on corrugated substrates [12, 104] of hexagonal and other symmetry. In a recent work [105] it was shown that in the complex interplay of density dependent settling rates with crystal compression and phase transition thermodynamics in addition to a plane interface with no depletion zones several shock fronts may evolve and their height in time can be described by a modified Kynch theory. For the freezing transition also there the WF-growth law may apply, albeit with strongly restrictive boundary conditions leading to a supply limited growth velocity under conditions of high settling rates.

Crystallization also may occur from amorphous solid phases. While no quantitative growth studies have been reported, it became clear that an expanding sediment formed by previous centrifugation will lead to homogeneously nucleated columns [106]. PMMA HS glasses show heterogeneous nucleation and growth from the sample top, while homogeneous bulk nucleation seems to be suppressed above $\Phi = 0.57$ [25]. Residues of the shear melting process, however, seem to provide possible heterogeneous nuclei and large oriented crystalline features are observed also in the bulk way above the glass transition [107].

4.3. Crystallization via homogeneous nucleation

This standard situation has received considerable interest. Smits *et al* investigated nearly hard spheres (coated Si in toluene/ethanol carrying some 260 charges/particle). There a maximum in the growth coefficient was reported at medium volume fractions [108]. For the pure HS case the growth law (cf table 1) was checked in SALS and BS experiments [70, 72, 109–111]. Assuming a finite induction time seems to work better than assuming a constant growth exponent. Well above melting the limiting exponents for WF growth are observed, while at lower packing fraction long lived transients with varying growth exponents are found which approximate diffusion limited growth for long times after nucleation. The appearance of these transient behaviour has successfully been modelled numerically [73–75], but, as shall be outlined below, it leaves data evaluation with a difficult task.

Very recently we tried to measure absolute growth velocities in an HS system using the apparatus sketched in figure 6(a) [66, 76]. We used PMMA/PHSA spheres of core size $a = 435$ nm and a coating of 10 nm thickness [112] in mixtures of decalin/tetralin. The polydispersity is $\sigma = 0.025$. These samples are a kind gift of W van Megen and S Underwood. We had access to five different Bragg peaks indexed (111), (200), (220), (311) and (222), as can be seen from figure 6. Interestingly, (200) is very pronounced, indicating a comparably low degree of random stacking and a clear preference for the fcc structure.

As explained above and in more detail in [66] and [76] application of the usual procedures to infer $S_C(q)$ from the raw data (cf figure 7 and [68]) was not applicable here. In short, the particles show a slight swelling with tetraline leading to an inhomogeneous profile of the refractive index. Their form factor therefore is very sensitive to small changes in solvent composition [112] and thus cannot be directly taken from experiments on diluted systems for the interpretation of growth experiments. We therefore adapted a different extraction procedure and divided the time dependent raw data by an early measurement, thus dividing out both the actual form factor and correcting for different sensitivity of the diodes. This however leads to severe distortions of $S_C(q)$ in those regions where $S_F(q)$ shows its pronounced oscillations and therefore excludes (111) and (200) from further evaluation. As further (222) is very weak,

only (220) and (311) were investigated in detail. As can be seen in figure 6(b), in their vicinity $S_F(q)$ only contributes a flat background, which can conveniently be subtracted before further integration.

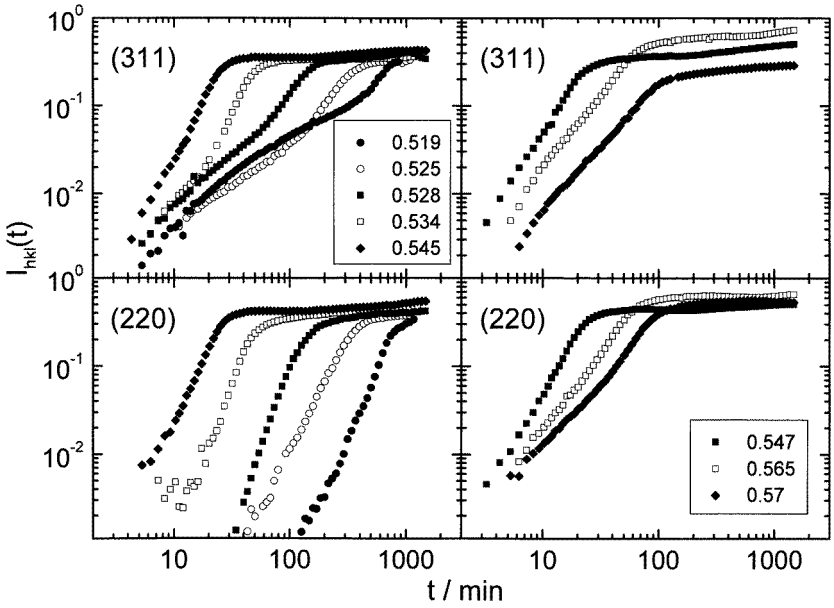

Figure 11. Time-dependent integrated peak intensities of (311) (top) and (220) (bottom) for PMMA890 at different packing fractions as indicated.

Integrated peak intensities I_{hkl} are given in figure 11 for different volume fractions. A qualitative different behaviour in the time dependence is immediately visible. While (220) data all show constant growth exponents (which are between 2.5 and 4 at low Φ), a second and lower growth exponent is observed for early times in the low volume fraction (311) data. A similar effect has been reported by Harland and van Megan [68] on the (111) reflection. There, however the effect was observed for high Φ data only and increased with increasing Φ. It was interpreted as a hindering of normal growth due to decaying shear residues which are most common in the highly viscous melts close to the glass transition. Only when these are dissolved may normal nucleation and growth commence to a significant amount. Note that a slight increase in α is also visible in our data on (220) for our largest packing fraction $\Phi = 0.57$.

We interpreted our low Φ data within an alternative approach, assuming shear residues to very quickly decay close to the phase boundary where diffusion is not yet strongly hindered. Resorting to the two dimensional scattering pattern we noticed the presence of sixfold symmetric intensity maxima in (311) and also (111) absent in (200) and (220). In a straightforward but nevertheless tricky crystallographic analysis these could be shown to result from wall nucleated crystals with a shear induced lateral orientation [66]. They do not actually hinder homogeneous nucleation but contribute to the integrated scattered intensity already during the induction time. The growth exponent for I_{311} of the sixfold symmetric pattern alone is close to one, which for diffusion limited growth in one dimension is the expected value for the maximum intensity at q_m, rather than for the integrated intensity which was measured here. Recalling the difficulties encountered in charged systems we refrain from further interpretation.

With increasing Φ this solidification mechanism loses importance. We note that, if induction times go through a minimum around melting [68], it may gain importance again as Φ_g is approached and an alternative interpretation of van Megen's data indeed may be an early low dimensional growth from bulk shear residues (stacks of (111) planes) of various orientations serving as nuclei. Their intensity contribution will become negligible, once the competing bulk homogeneous nucleation starts. Further experiments should clarify this issue.

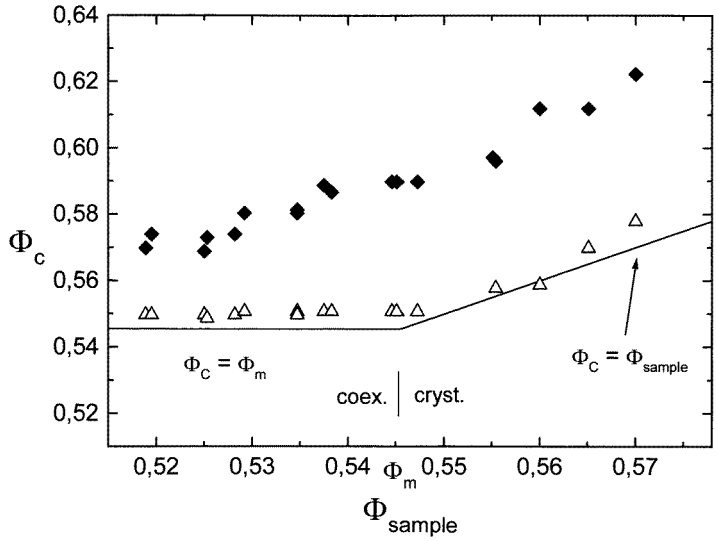

Figure 12. Crystal packing fractions Φ_C of PMMA890 at $t \approx t_i$ (♦) and at large times $t = 1000$ min (△). The solid line indicates the theoretical expectations for Φ_C at $t \to \infty$.

For evaluation of growth after homogeneous nucleation therefore in our system only (220) and the small angle data (cf figure 6(c)) are left. In each of the data sets the intensity rises strongly after some induction time t_i. After complete solidification ($\sim$30 min for $\Phi = 0.545$) intensity changes are much weaker, nevertheless indicating further ripening. Throughout solidification we observe a continuous shift in the position of the BS maxima. Figure 12 compares the derived crystal packing fractions at the first appearance of Bragg peaks to those observed in the limit of very long times. We conclude the crystals to nucleate in a compressed state and to slowly expand. Solidification becomes generally faster with increasing concentration across the coexistence regime but slows down again above melting. Except for samples with Φ slightly above Φ_m, also in our experiments strong temporal variations in velocity and growth exponent are observed. The interpretation of the complete time dependent kinetics thus becomes very difficult and is restricted to early times.

Crystal sizes were determined from peak widths as described above. For short times the size evolved roughly linearly for both SALS and BS data (cf figure 8(a)). We thus could derive an apparent short time velocity. Figure 13(a) shows the results. For sublinear growth (as expected below melting for diffusion limited growth and way above melting for the above mentioned transient behaviour) this procedure underestimates the true initial growth velocity. Figure 13(b) compares the logarithm of these apparent velocities to a WF law using $v = K D_{eff}(\Phi)/d_{NN}[1 - \exp(-\Delta\mu(\Phi)/k_B T)]$ where d_{NN} is the mean particle distance and D_{eff} and $\Delta\mu$ are taken from experiment [25] and theory [93, 94], respectively. As the figure contains data taken from both experiments it again demonstrates consistency of results (see also [110]). In this approach the theoretical growth velocity shows a maximum at about

$\Phi \approx 0.515$. The experimental data show a maximum around $\Phi \approx 0.535$ and lie above the theoretical prediction for v. Most of our data can be fitted with $K = 40$. This leads to an upward shift of the curve while the functional form is retained. Roughly speaking, each particle attaching to the crystal has to move over a distance on the order of $1/40$ of the interparticle distance, which is on the order of the distance between particle surfaces.

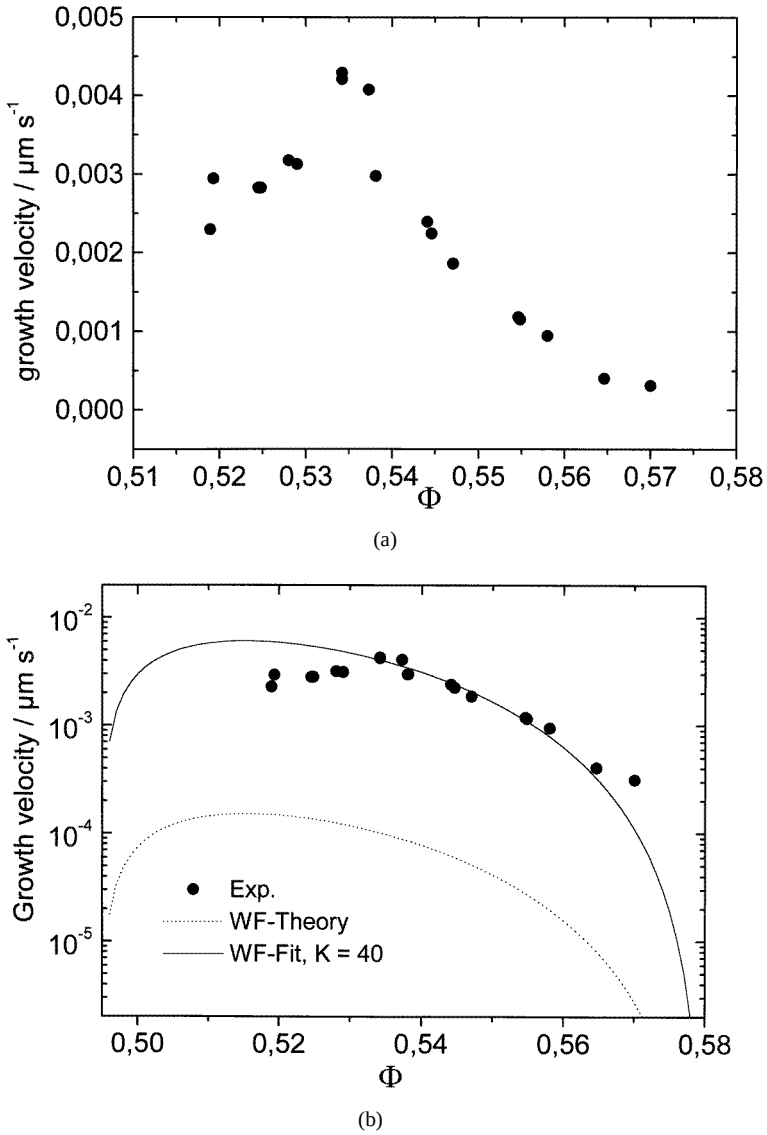

Figure 13. (a) Apparent growth velocities v for PMMA890; (b) the same plotted in a semi-logarithmic way to compare to WF predictions.

The predicted functional form is met between melting and the glass transition, while deviations toward significantly lower values are observed below melting and a much too large value for the sample at $\Phi = 0.57$. The former may be expected, as below melting in HS systems two kinetic processes are responsible for the growth velocity, namely the self-diffusion of a

particle towards its target place in the crystal and the preceding transport towards the interface which may be much slower or over longer distances and in fact limit v. The latter may be expected from the results of exhaustive computer simulations of fcc/melt interfaces [34], where even for $T^* = 0$ growth was facilitated through the release of latent heat and local density variations provided by the density difference between crystal and melt. Since here experiments are performed at room temperature particles will move once local decrease in density allows for further motion. A further interpretation of absolute velocities is feasible only in comparison to the soft sphere data and shall be pursued below. For the moment we state that our data are not inconsistent with a WF-growth law, where it is actually expected.

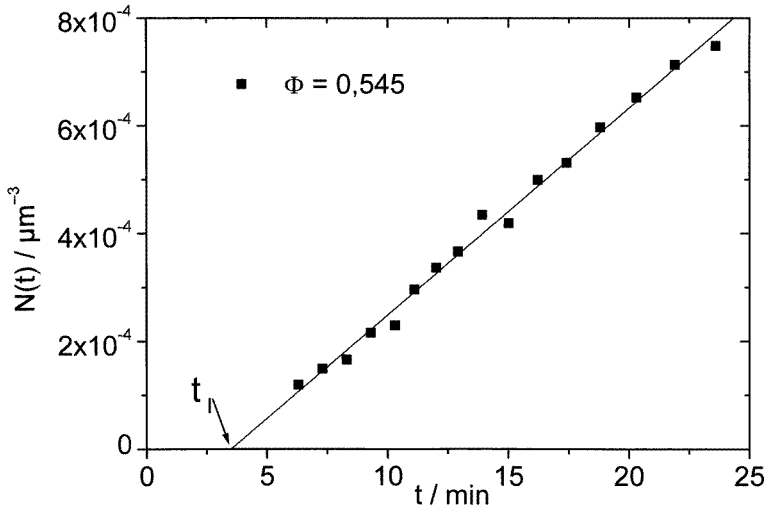

Figure 14. Number density $N(t)$ of crystallites in the scattering volume. PMMA890, $\Phi = 0.545$.

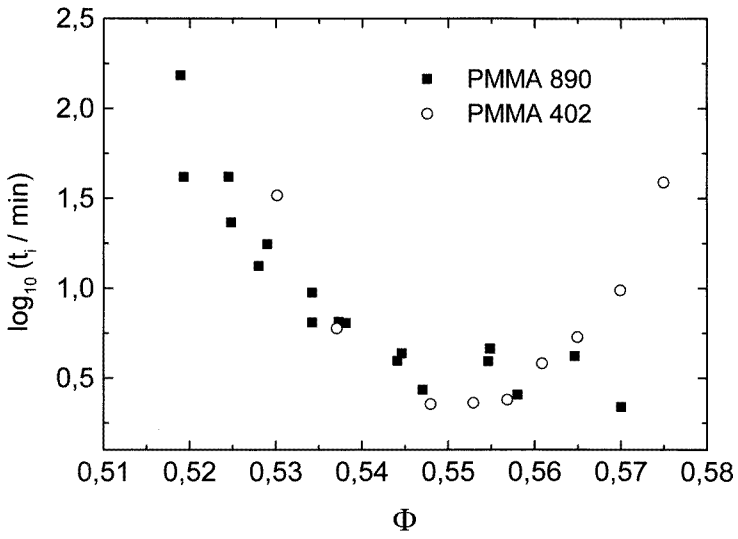

Figure 15. Induction times t_i for PMMA890 (■) and PMMA402 (○) [68].

Knowing the crystallite radii, the number of average sized crystals $N(t)$ in the scattering volume may be determined from the integrated intensity. Figure 14 shows this value for the sample at $\Phi = 0.545$. No crystallites are observed up a certain time t_i, the induction time, then for practically all samples N increases linearly. Figure 15 compares results on t_i to the data of Harland taken on particles of about half the size (PMMA402). Induction times are very similar for both systems; however the pronounced minimum present in Harland's data is not observed in our case. The reason for this discrepancy is not yet understood. We note that above $\Phi \approx 0.55$ Harland's data follow the inverse of the long time diffusion coefficient.

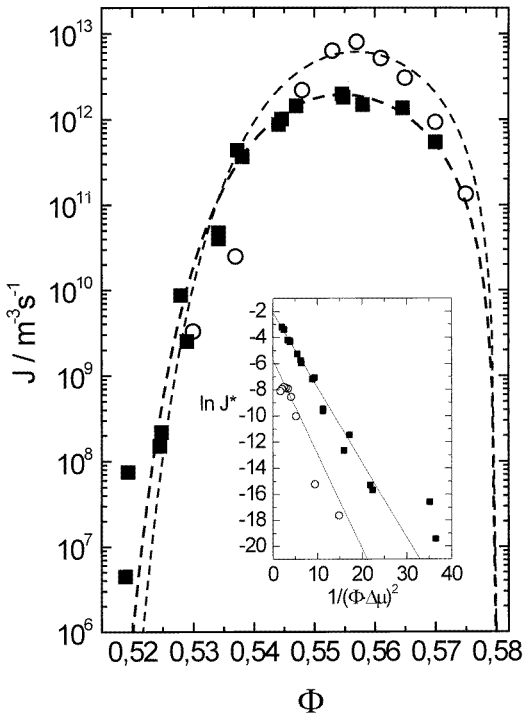

Figure 16. Comparison of nucleation rate densities J of PMMA890 to PMMA402 (from [68]). Symbols as in figure 15. Dashed lines are theoretical fits to the data for PMMA890 and PMMA402. The inset shows the dimensionless nucleation rate densities J^* plotted logarithmically versus $1/(\Phi\Delta\mu)^2$.

From $\mathrm{d}N(t)/\mathrm{d}t$ and the scattering volume $V_S = 0.25 \times 10^{-6}$ m^3 the absolute nucleation rate density is derived and compared in figure 16(a) to theory and Harland's data. The latter were calculated from the dimensionless nucleation rates given by the authors. As D_0 is not known for Harland's data we calculated it from the Brownian time given in their paper $\tau_B = a^2/D_0 = 0.047$ s to be 8.122×10^{-13} m^2 s^{-1}. Interestingly both data sets fall upon each other within one order of magnitude. The most surprising fact is that these samples of much higher number density and much smaller radius nevertheless show roughly the same nucleation rate density as our samples. Also shown are theoretical curves for $J = K(nD_0(1 - \Phi/0.58)^{2.58}/l^2)\exp(-\Delta G^*/k_BT) = K(D_{eff}\Phi^{5/3}/(4\pi/3)^{5/3}a^5)\exp(-\Delta G^*/k_BT)$ with the typical length l given in units of the inter-particle distance $d_{NN} = n^{-1/3}$. The inset gives the same curves in dimensionless units $J^* = J/J_0 = J/(D_{eff}\Phi^{5/3}/(4\pi/3)^{5/3}a^5)$ plotted versus $1/(\Delta\mu n)^2$. Then the ordinate gives $\ln(K)$ and the surface tension γ can be inferred from the slope $\mathrm{d}\ln(J)/\mathrm{d}(\Phi\Delta\mu)^2 = 4\pi^3\gamma^3/27$.

Two independent fit parameters enter: the choice of the dimensionless surface tension $\gamma^* = 4\gamma a^2/k_BT$ very sensitively determines the functional form via G^*, while the variation in l only shifts the curves. Except for the points at lowest volume fraction the theoretical curve can be well fitted to the experimental data of PMMA890. Deviations at low Φ possibly result from impurity nucleation. As can in particular be seen from the insert the fit for PMMA402 is less good and the data seem to become independent of metastability at large Φ. The best fits are $\gamma^* = 0.50 \pm 0.01$ for PMMA890 and $\gamma^* = 0.54 \pm 0.03$ for PMMA402. Both are compatible with each other and with the recent analysis of Marr [113], considerably larger than recent results from density functional theory [38] and somewhat smaller than older results of Marr and Gast.

The second fit parameters $K_{402} = 0.0034 \pm 0.0015$ and $K_{890} = 0.126 \pm 0.013$ indicates that nucleation is significantly slower than estimated by this simple theory. Further, the nucleation rate is grossly different for the two samples. If deviations of K from one are expressed in distances from the target place, PMMA890 particles have to diffuse $2.8d_{NN}$, while PMMA402 particles need some $17d_{NN}$ for $\Phi > \Phi_m$ and even more in the coexistence regime. As PMMA890 has a polydispersity of $\sigma = 0.025$ and PMMA402 of $\sigma = 0.05$, it is tempting to ascribe the difference to the larger polydispersity. The physical picture behind this could be the following. Polydispersity will enhance the energy barrier, as the latent heat will be lower for a less well ordered nucleus, and thus significantly reduce the number of critical nuclei composed of differently sized particles. Assuming nucleation being possible only for sufficiently monodisperse fractions or local environs, $17d_{NN}$ would correspond to the mean distance of suitable particles from a possible nucleation site.

5. Solidification in charged sphere suspensions

5.1. Preparation and conditioning

Also here important experiments have been reported mainly through the use of novel preparation techniques and advanced microscopic methods. Charged particles are available commercially or synthesized after different recipes with a wide variety of sizes, polydispersities, different surface groups and charge densities. Different methods of particle sizing are indicated [114, 115]. Main features of systems reviewed here are compiled in table 2.

Practically all of the suspension properties can be described well using a Debye–Hückel type potential. Charge numbers used therein, however are often considerably smaller than the number of titrated surface groups. It thus became customary to discuss the interaction in terms of an effective charge and to attribute the observed deviations to incomplete dissociation, counter-ion condensation of the Manning type [26, 117, 118] and other mechanisms. Effective charges Z_i^* can be determined from a number of techniques. We here derived them from the BS calibrated n-dependency of the conductivity of deionized samples known to be independent of the system structure [48] via:

$$\sigma = enZ_\sigma^*(\mu_H^+ + \mu_P^-) + \sigma_B \tag{19}$$

where $\sigma_B \approx 60$ nS cm^{-1} is the background conductivity of water and e is the elementary charge. Proton mobilities $\mu_H^- = 36.5 \times 10^{-8}$ m^2 V^{-1} s^{-1} are taken from literature and particle mobilities $\mu_P^- = (2\text{–}20) \times 10^{-8}$ m^2 V^{-1} s^{-1} are measured independently [119].

Effective charges may also be calculated in a two step procedure using a program kindly provided by Luc Belloni [120]. First the non-linearized Poisson–Boltzmann equation is solved numerically in a spherical Wigner–Seitz cell under charge regulation boundary conditions. In dependency on the particle size, number of titrated groups N, surface pK, particle number

Table 2. Particle properties of the samples investigated. d: nominal diameter given by manufacturer; a: geometrical radius; σ: polydispersity; determination via: transmission electron microscopy (TEM), dynamic light scattering (DLS), static light scattering with contrast variation (SLS/CV), forced Rayleigh scattering (FRS); data for PMMA402 are taken from [68]; N: titrated number of surface groups; $Z^*(\sigma)$, effective charges as derived from conductivity via equation (19).

	Batch No	d (nm)	a (nm)	σ	N	$Z^*(\sigma)$
PS120	IDC	120	Turbidity	DLS	3.6×10^3	685
	10-202-66		59	0.038	Sulphate	
PS109	Seradyn	109	Turbidity	FRS	950	395
	2011 M9R		51	0.015	Sulphate	
PS109*	Seradyn	109	Turbidity	FRS	1200	450
	2010M9R		51	0.015	Sulphate	
PS91	Serva	91	TEM	DLS [116]	5.9×10^3	800
	41907		35	0.01	Sulphate	
PMMA890		—	SLS/CV	SLS/CV	PMMA/	—
(SMU28)			445	0.025	PHSA	
PMMA402		—	SLS	DLS	PMMA/	—
			201	0.05	PHSA	

density, and concentration c of added 1:1 electrolyte, the electrostatic potential $\Psi(r)$ is calculated. Then, following the suggestions of Alexander *et al* [117] a Debye–Hückel type potential

$$\Psi^*_{DH}(r) = \frac{Z^*_{DH} e}{4\pi\varepsilon} \left(\frac{\exp(\kappa a)}{1 + \kappa a} \right) \frac{\exp(-\kappa r)}{r} \tag{20}$$

is fitted to the full solution at the Wigner–Seitz cell boundary with the Debye screening parameter:

$$\kappa = \frac{e^2}{\varepsilon k_B T} \sqrt{n Z^*_{DH} l^2 + n_S l^2} \tag{21}$$

and Z^*_{DH} as free parameter. Here $\varepsilon = \varepsilon_0 \varepsilon_r$ is the dielectric permittivity of water and n_S is the number density of salt ions. Except for extremely high surface charge densities results of this mean field treatment (also termed charge renormalization) compare favourably to those obtained from more sophisticated approaches. We note that while other experiments may yield significantly different values for Z^*_i [48, 117, 121, 122], Z^*_σ usually agrees well with Z^*_{DH} and for PS120 $Z^*_{DH} = 730$.

Particle number densities are obtained from scattering data on crystalline samples (cf figure 5) or from conductivity, where no scattering data are available. The salt concentration is adjusted by ultra-filtration, dialysis or addition of known quantities of salt after thorough deionization. In particular in the latter case care has to be taken to avoid contamination with dissolving CO_2 and to exclude the ion exchange resin from the actual measuring cell to avoid particle transport due to diffusiophoresis. Such preparation artefacts may alter the phase behaviour [123]. Cycling the suspension peristaltically through a closed tubing system which connects different components (ion exchange chamber, conductivity measurement, structure measurement etc) has proven suitable to guarantee gradient free, homogeneous shear melts and reproducible adjustment of control parameters within short times. This technique is also employed here. Details of this procedure are given elsewhere [68, 121]. We just note that residual uncertainties in n, c and Z^*_σ are less than 2%, if the temperature is controlled to some 0.1 °C.

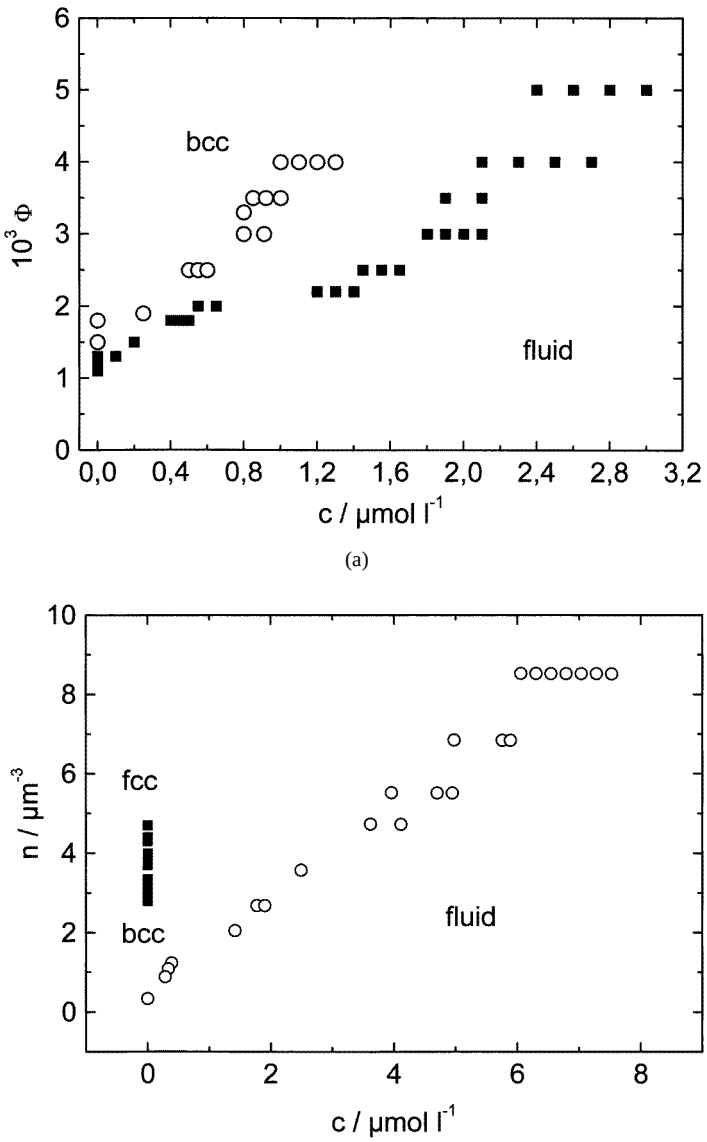

Figure 17. Coexistence regions in the phase diagrams of (a) PS109 (○) and PS109* (■); (b) PS120: bcc/fcc (■); bcc/fluid (○).

5.2. Phase behaviour and morphology

Matching the refractive indices to that of water or ethanol is difficult as $\nu_{PS} = 1.559$ and $\nu_{SI} = 1.463$. Only for PTFE ($\nu_{PTFE} = 1.3560$) is this possible with the fine tuning performed by adding small amounts of urea [124]. Therefore highly concentrated samples appear turbid and x-ray crystallography is employed to study the full range of the *n*–*c*-phase diagram [125]. At sufficiently low *c*, however also low *n* samples show fluid, bcc and fcc order [126–128] in near quantitative agreement with computer simulations [26, 129] and perturbation

theoretical treatments [130]. Also amorphous phases were reported [131, 132] and predicted [133]. In two component systems the formation of glasses, alloys and crystals [134] sometimes with interstitially mobile small components were observed [135]. We just note that in addition some experiments seem to indicate the possibility of phase segregation phenomena [136] or the formation of metastable crystals from very low concentration samples [137]. The origin of this, however is still discussed controversially [138].

For the particle discussed here in more detail figure 17(a) and (b) give the phase diagrams [44, 48]. At low density and low salt the suspension is more OCP-like and a bcc structure is formed while for the more HS-like case with stronger screening an fcc structure is observed. In figure 17(b) the coexistence range between bcc and fcc is much broader than between fluid and bcc. It is not known as yet whether this is due to size polydispersity which may have a stronger influence at larger screening. In fact, it has not been systematically studied how size and charge polydispersity are related and only a few suggestions exist. For strictly monodisperse systems with all degrees of freedom of the counter-ions coupling to the particle position the coexistence regime actually is predicted to vanish [139], an assumption which probably is not fulfilled for these systems. We note that for charge variable particles at constant Φ the position of the phase boundary in an N/c-diagram becomes nearly independent of the surface group number for sufficiently large N. This has been interpreted in terms of a saturation in the effective charge Z^* [128] (also cf [140]).

A particularly nice feature of charged suspensions is the fact that crystals wet a charged wall, leading to the formation of heterogeneously nucleated crystals oriented with their closest packed plane parallel to the wall [141]. Studies of crystal formation in narrow slit geometries show that first a fluid layer is formed which then crystallizes [12, 142]. Thus the nucleation mechanism was identified to be layering mediated. Under shear hexagonal layers appear which are further oriented to either have the closest packed direction parallel (large amplitude shear) or perpendicular (low amplitude oscillatory shear) to the flow direction [143–145]. After cessation of shear, stacking faulted growth of otherwise single crystals results for fcc. Also bcc can nucleate from shear induced hexagonal layers; the detailed mechanism, however, remains unresolved. As can be seen in figure 7(b) a typical morphology is a pattern of columnar twin domains [86]. While in thick cells homogeneous nucleation dominates, wall nucleation yielding a flat interface may be made dominant by using moderately deep quenches and thin flat flow through cells.

5.3. Growth

Aastuen *et al* were the first to find strong indications of WF growth above melting in experiments varying n at constant $c \approx 0$ using BM on samples with ion exchanger present in the cell. Similar in spirit to defining a reduced undercooling T^* in atomic melts they approximated the difference in chemical potential by $\Delta\mu = B(n - n_f)/n_f$; f and m denote freezing and melting, respectively. They found the proportionality constant $B \approx 8\ k_B T$ and the radially averaged limiting velocity $\bar{v}_\infty = 17\ \mu\text{m s}^{-1}$ [83]. Würth *et al* [88] used the set-up sketched in figure 10(a) to study slightly larger particles of two different effective charges under variation of salt concentrations and densities (conditioning after [67]). Below melting very low and eventually slowing growth velocities v_{110} were observed while linear growth was found above melting. In each series the increase in the growth velocity covered some two orders of magnitude before the saturation value of $v_{110} = 9.1\ \mu\text{m s}^{-1}$ was reached (figure 18(a), (b)). All data should collapse on a single curve if in the approximation used for $\Delta\mu$ the pair potential is properly accounted for. The authors defined an energy density $\Pi = \alpha n V(r)$, where α is an

effective nearest neighbour number and the pair energy of interaction was approximated as:

$$V(r) = \frac{Z^{*2}e^2}{4\pi\varepsilon}\left(\frac{\exp(\kappa r)}{1+\kappa r}\right)^2 \frac{\exp(-\kappa r)}{r}. \tag{22}$$

This allowed them to estimate a dimensionless rescaled energy density $\Pi_m^* = (\Pi - \Pi_m)/\Pi_m$. In fact, as is shown in figure 19 all data of figure 18 collapse on a single curve, indicating the validity of the simple rescaling procedure. Further, the data could be well fitted with equation (1) with $B = (6.7 \pm 0.7)\ k_B T$. Note that in figure 19 data taken at coexistence have negative Π_m^*-values. The authors pointed out that their thermodynamically somewhat inconsistent choice of melting as reference point was motivated by the better fit of equation (1). However, using

$$\Delta\mu = B\Pi_f^* = B\left(\frac{\Pi - \Pi_f}{\Pi_f}\right) \tag{23}$$

for the energy gain upon crystallization per particle gives very similar results only the uncertainty is somewhat worse.

We recently repeated these experiments on the slightly more polydisperse sample PS120. Microscopy data taken in dependency on Φ show a broader scatter due larger contamination with spurious small ions in the particular cell used. Velocities at $n < 2.56\,\mu\mathrm{m}^{-3}$ were too small to be determined accurately. Further the sample reveals a considerably broadened coexistence region presumably due to polydispersity. Nevertheless, again a strong increase in v_{110} close to the phase boundary and a saturation at a value of $v_\infty = 3.9\ \mu\mathrm{m\ s}^{-1}$ are clearly observed. The raw data are shown in figure 20. Fits of equation (1) using Π_f^* give $B = (5.8 \pm 1.9)\ k_B T$ while using Π_m^* yields a B-value of the order of $10\ k_B T$ with a considerably larger uncertainty [86].

To treat all available data on a common footing, we replot our and Aastuen's data on CSs in terms of $\Delta\mu$ in figure 21, where for each sample the B-values compiled in table 3 are used. For PS91 B is taken from Aastuen *et al*. We also show plots of $v = v_\infty[\exp(-B\Pi_F^*/k_B T)]$ with v_∞ and B compiled in table 3. Arrows in figure 21 give the melting value of $\Delta\mu$ for PS109 (left) and PS120 (right); freezing, of course, is at $\Delta\mu = 0$.

Concerning the functional form, we notice that close to the phase transition the velocity for PS120 is significantly smaller than expected after WF. The strong increase is observed around melting. Note that also Würth's data show this trend but masked by the narrowness of the coexistence region in their case of less polydisperse particles. As before in the HS case we can only suspect a difference in growth mechanism to be responsible for the observed scenario. Below melting density changes have to occur in addition to structural rearrangements. This cannot, of course, be understood solely in terms of a single diffusion coefficient. From our observations we nevertheless find that above melting the WF law is fulfilled in all three soft sphere samples.

We finally compare the results of figure 13(a) and (b) to those of figure 21. In both HSs and CSs the region of validity for WF growth was identified to extend from around melting to large degrees of metastability. It is interesting to recall that a chemical potential difference of $1\ k_B T$ corresponds to $2.5\ \mathrm{kJ\ mol}^{-1}$ crystallization free energy. Further, in colloidal systems the latent heat release varies with the variation of pair potential and density, while the temperature stays practically constant due to the excellent thermal reservoir of the carrier liquid. Table 3 compiles estimates of the maximum molar free energy differences between melt and solid. Evidently investigations of CSs cover a considerable range of transition free energies well comparable to atomic substances.

Nevertheless the growth velocities are orders of magnitude smaller than for atomic melts, differ significantly for individual systems and, in fact, no clear limiting velocity is observed for

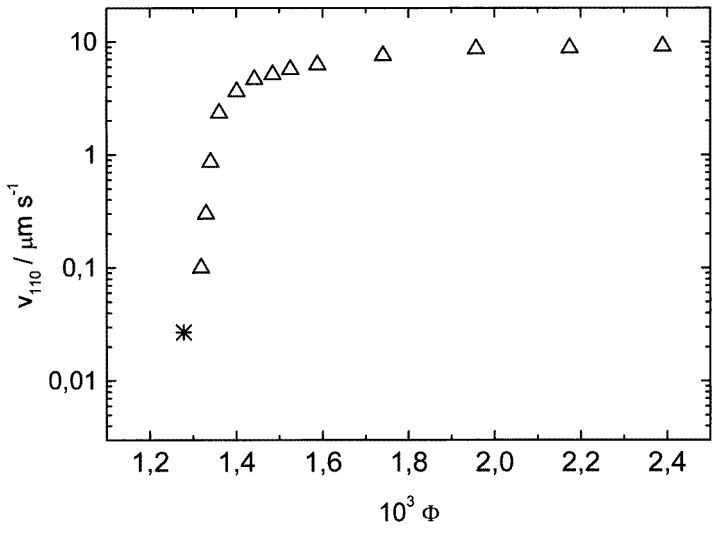

(a)

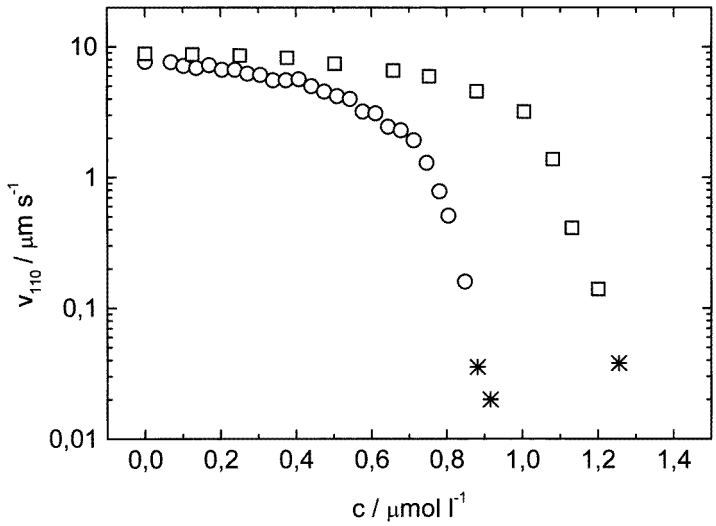

(b)

Figure 18. Growth velocities of (a) PS109* at $c = 0$ μmol l^{-1}, (b) PS109 at $\Phi = 0.003$ (○) and PS109* at $\Phi = 0.0022$ (□). Stars denote points taken at coexistence.

HS. Thus the interesting open question arises, whether a common description for the kinetic prefactor v_∞ can be derived. From the analysis of dimensions it should be proportional to a frequency times a length scale. Assuming a flat interface between crystal and adjacent homogeneous melt the length scale will correspond to the interfacial thickness d_I. The frequency is derived from the ratio of a diffusion coefficient and the square of a second length scale l, which for instance may equal the mean distance of a particle just outside the moving interface from its final target place again just outside the interface, but now on the crystal side. Since the prediction of absolute prefactors has to rely on the right choice of diffusion constants

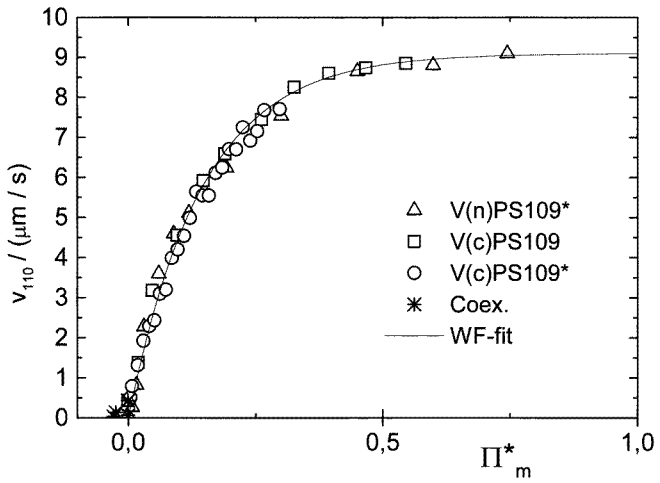

Figure 19. Growth velocities for both PS109 samples plotted versus dimensionless rescaled energy density $\Pi^*_m = (\Pi - \Pi_m)/\Pi_m$. Symbols as in figure 18. The solid line gives a WF fit with $v_\infty = 3.9\ \mu\text{m s}^{-1}$. The fit parameter K is given for two different formulations of v^*.

Table 3. Compilation of results on available growth data.

	B $[k_BT]$	$N_A\Delta\mu_{MAX}$ [kJ mol^{-1}]	v_∞ [μm s^{-1}]	$v^* = v_\infty d_{NN}/D_{eff}$ K	$v^* = v_\infty a/D_{eff}$ K
PS91	8	35	17	15	1.6
PS109	6.7	40	9.1	12	0.97
PS120	5.8	13	3.9	14	0.55
PMMA890	—	1.2	4.3×10^{-3}	27	14.5

and length scales as well as on structural details of the interfacial region, we can only illustrate this important problem, rather than solve it.

A specific question is the choice of the diffusion coefficient. In the case of HSs we used the long time self-diffusion coefficient D_{eff} measured experimentally to find a good qualitative agreement between growth data and WF prediction. One may however also argue for the short time self-diffusion coefficient, since the particle may not have to leave its cage, or for the collective diffusion coefficient measured at the maximum of $S(q)$, since we consider a structural rearrangement of the local cage. If e.g. we chose the simplest approximations $D = D_0$, $l = a$ and $d_I = 2a$, v_∞ should decrease with increasing particle size and be independent of packing fraction as qualitatively observed in figure 21. In particular for HSs a more appropriate choice may be $D = D_{eff}(\Phi)$. Further setting $l = d_I = d_{NN}$ results in $v_\infty \propto D_{eff}/d_{NN}$. To compare HSs to CSs we replot in terms of reduced growth velocities with $v^* = vd_{NN}/D_{eff}$. Thus, in each data series we rescaled the absolute growth velocity by multiplying with the inter-particle distance and dividing by the effective diffusion coefficient which allows comparison to a WF law with constant limiting velocity $v_\infty = 1$. For the HS data we again used $D_{eff} = D_0(1-\Phi/0.58)^{2.58}$ [25, 68] and for the CS we used the dynamic freezing criterion of Löwen, Simon and Palberg to estimate $D_{eff} = 0.1D_0$ [146, 147]. The results are shown in figure 22. Data are compared to $v^* = K(1 - \exp(-\Delta\mu/k_BT))$ and the results for the fit parameter K are compiled in table 3. Note that PS120 data do not follow the functional form of the fit curve over the whole range of parameters, possibly indicating a decrease in

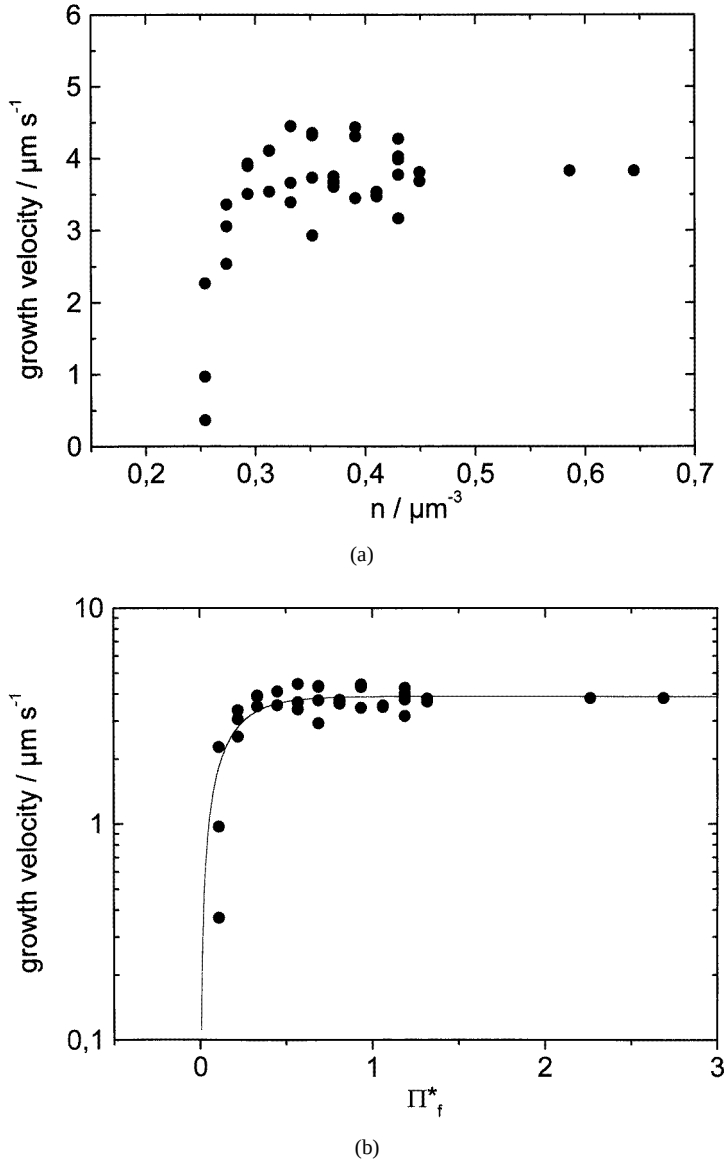

Figure 20. Growth velocities for PS120. (a) v versus particle number density n; (b) v plotted semi-logarithmically versus Π_f^* calculated using equation (23). The solid curve is the best fit of a WF law yielding $B = (5.8 \pm 1.9)\ k_B T$ and $v_\infty = 3.9\ \mu\text{m s}^{-1}$.

D_{eff}.

The most striking feature is the closeness of rescaled velocities for the different systems. The spread in packing fractions and observed absolute growth velocities in the original data contained several orders of magnitude. Now limiting velocities are less than a factor of two apart for CSs and the K-values show no clear correlation with particle radius nor polydispersity. The HS K is only a little larger, while the HS particle radius is larger by a factor of about eight. In table 3 we also show the results for an evaluation using $v^* = va/D_{eff}$. There the spread in

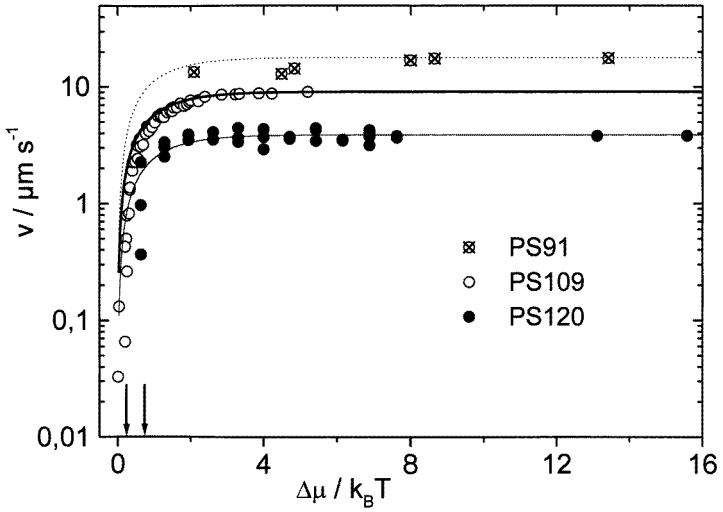

Figure 21. Comparison of CS growth velocities plotted versus $\Delta\mu$. The limiting velocities decrease with increasing radii. Arrows indicate $\Delta\mu_m$ (right: PS120; left: PS109). Symbols as indicated.

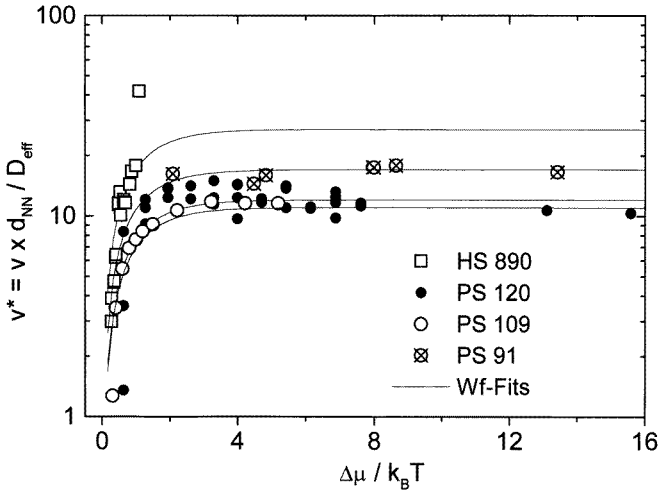

Figure 22. Comparison of CS to HS growth in terms of the dimensionless growth velocity v^* versus $\Delta\mu$. Fit parameters for WF fits are compiled in table 3. Symbols are as indicated.

limiting velocities for CSs is still present with large spheres having lower K values.

From these comparisons we conclude that using the inter-particle distance for scaling seems more appropriate than using the particle radius. Note, however, that d_{NN} approaches $2a$ in the HS case. Further, growth in different CS systems is very similar and possibly not too different from the HS case. The absolute value for K in figure 22 should be 1 if the interfacial thickness is one monolayer and the particles have to diffuse one particle distance with D_{eff}. Values of about ten can be explained by a faster diffusion (here $D_{eff} = 0.1D_0$), a shorter way to the target place (see [88]) or layering with an increase in d_I, where computer simulations indicate values of a few d_{NN} [6]. We currently cannot discriminate between these

alternatives. Direct microscopic studies should prove very helpful to clarify this issue which certainly deserves further experimental attention.

6. Conclusion

We have presented measurements of the basic processes of nucleation and growth of colloidal crystals from their melts. A variety of sophisticated experimental methods was demonstrated to give valuable information on both problems through the combination of direct observation in real space and the analysis of scattering patterns. The connection between experimental parameters like packing fraction or for CS density, charge and salt concentration to thermodynamic properties was successfully achieved through computer simulations, theory or semi-empirical calibration methods. A general qualitative agreement between classical concepts of nucleation and growth with our and other authors' measurements on purely repulsive systems was observed. In growth appropriate scaling allowed for the comparison of hard and soft sphere data. A full quantitative understanding of the kinetic prefactors and of the kinetic laws in the coexistence region still has to be developed. Here the knowledge of detailed mechanisms is of great importance to identify the relevant diffusion coefficients and length scales.

Up to now the basic features of classical solidification theories were confirmed for purely repulsive systems. Important developments are awaited for ripening, for nucleation and growth far from mechanical equilibrium or in thin films, for the competition between crystallization and glass formation or phase separation and for solidification in mixed systems where at small differences in radii alloy formation and at large differences phase separation will prevail. In any of these cases colloids will provide suitable model systems, but theoretical calculations and simulations can support the understanding of the solidification kinetics to an extent rarely encountered with other condensed matter problems. This finally aims back at a refined understanding of manufacturing processes for example in diffraction optical and acoustic devices, optical band gap materials or novel coating materials.

Acknowledgments

It is a pleasure to thank those who actually have performed the experiments in the group of P Leiderer in Konstanz and in our group in Mainz: A Heymann, J Kottal, M R Maaroufi, H-J Schöpe, J Schwarz, A Stipp and M Würth. The paper profited from numerous valuable discussions with H Löwen, M Ballauff, W van Megen and P Leiderer. We are indebted to M Evers and M Ballauff for their critical reading of the manuscript. Financial support of the DFG (SFB 306, SFB 262, Pa459/6-3, Pa459/8-1, Scha389/6-1,2) of the Materialwissenschaftliches Forschungszentrum Mainz (MWFZ) and of the HCM colloid physics network are gratefully acknowledged.

References

[1] Kepler J 1611 *Strena seu de nive Sexangula* (Frankfurt)
[2] Herlach D M, Cochrane R F, Egry I, Fecht H J and Greer A L 1993 *Int. Mater. Rev.* **38** 273
[3] Kelton K F 1993 *Solid State Physics* vol 45 (New York: Academic) p 75
[4] Gilmer G H 1993 *Handbook of Crystal Growth* vol 1, ed D T J Hurle (Amsterdam: Elsevier) p 585
[5] Oxtoby D W 1992 *J. Phys.: Condens. Matter* **4** 7627
[6] Löwen H 1994 *Phys. Rep.* **237** 249
[7] Ackerson B J (ed) 1990 *Phase Transitions* **21** (2-4)

[8] Palberg T 1997 *Curr. Opinion Colloid Interface Sci.* **2** 607
[9] Rutgers M A, Xue J-Z, Herbolzheimer E, Russel W B and Chaikin P M 1995 *Phys. Rev.* E **51** 4674
[10] Pusey P N 1991 *Liquids, Freezing and Glass Transition, 51st Summer School in Theoretical Physics (Les Houches, 1989)* ed J P Hansen, D Levesque and J Zinn-Justin (Amsterdam: Elsevier) p 763
[11] Sood A K 1991 *Solid State Physics* vol 45 (New York: Academic) p 1
[12] Crocker J C and Grier D G 1998 *MRS Bull.* **23** 24
C Murray 1998 *MRS Bull.* **23** 33
van Blaaderen A 1998 *MRS Bull.* **23** 39
Asher S A, Holtz J, Weismann J and Pan G 1998 *MRS Bull.* **23** 44
[13] Dingenouts N and Ballauff M 1998 *Macromolecules* **31** 7423
[14] Hansen J P and MacDonald I R 1986 *Theory of Simple Liquids* (London: Academic)
[15] Egelstaff P A 1992 *An Introduction to the Liquid State* (Oxford: Clarendon)
[16] Coussaert T and Baus M 1995 *Phys. Rev.* E **52** 862
[17] Tejero C F, Daanoun A, Lekkerkerker H N W and Baus M 1995 *Phys. Rev.* E **51** 558
[18] Likos C N, Nemeth Zs T and Löwen H 1994 *J. Phys.: Condens. Matter* **6** 10 965
[19] Hagen M H J, Meijer E J, Mooij G C A M, Frenkel D and Lekkerkerker H N W 1993 *Nature* **365** 425
[20] Baus M 1987 *J. Stat. Phys.* **48** 1129
[21] Wood W W and Jacobson J D 1958 *J. Chem. Phys.* **27** 1207
Alder B J and Wainwright T E 1958 *J. Chem. Phys.* **27** 1208
[22] Vroege G J and Lekkerkerker H N W 1992 *Rep. Prog. Phys.* **55** 1241
[23] Poon W C K and Pusey P N 1995 *Observation, Prediction and Simulation of Phase Transitions in Complex Fluids* ed M Baus *et al* (Amsterdam: Kluwer) p 3
[24] Pusey P N and van Megen W 1989 *Nature* **320** 340
[25] van Megen W 1995 *Transport Theory Stat. Phys.* **24** 1017
[26] Robbins M O, Kremer K and Grest G S 1988 *J. Chem. Phys.* **88** 3286
[27] Pusey P N, Poon W C K, Ilett S M and Bartlett P 1994 *J. Phys.: Condens. Matter* **6** A29
[28] Lekkerkerker H N W, Dhont J K G, Verduin H, Smits C and van Duijneveldt J S 1995 *Physica* A **213** 18
[29] vanRoij R and Hansen J P 1997 *Phys. Rev. Lett.* **79** 3082
[30] Hobbie E K and Holter M J 1998 *J. Chem. Phys.* **108** 2681
[31] Becker R and Döring W 1935 *Ann. Phys., Lpz.* **24** 719
[32] Turnbull D and Fisher J C 1949 *J. Chem. Phys.* **17** 71
[33] Wilson H A 1900 *Phil. Mag* **50** 238
Frenkel J 1933 *Z. Sowjetunion* **1** 498
[34] Burke F, Broughton J Q and Gilmer G H 1988 *J. Chem. Phys.* **89** 1030
[35] Cahn R W and Haasen P 1996 *Physical Metallurgy* (Amsterdam: North-Holland). In particular H Biloni and W J Boettinger p 669
[36] Banfi G, Degiorgio V, Rennie A R and Barker J G 1993 *J. Appl. Phys.* **74** 6925
[37] Jackson K A 1968 *Prog. Solid State Chem.* **4** 53
[38] Ohnesorge R, Löwen H and Wagner H 1994 *Phys. Rev.* E **50** 4801
Kyrilidis A and Brown R A 1995 *Phys. Rev.* E **51** 334
[39] Honeycutt J D and Andersen H C 1986 *J. Phys. Chem* **90** 1585
[40] Cape J N, Finney J L and Woodcock L V 1981 *J. Chem. Phys.* **75** 2366
[41] Swope W C and Andersen H C 1990 *Phys. Rev.* B **41** 7042
[42] TenWolde P R, Ruiz-Montero M J and Frenkel D 1996 *J. Chem. Phys.* **104** 9932
[43] van Duineveldt J S and Frenkel D 1992 *J. Chem. Phys.* **96** 4655
[44] Palberg T, Würth M, Simon R and Leiderer P 1994 *Prog. Colloid Polym. Sci.* **96** 62
[45] Simon R, Palberg T and Leiderer P 1993 *J. Chem. Phys.* **99** 3030
[46] Nägele G 1996 *Phys. Rep.* **272** 217
[47] Ackerson B J 1990 *J. Rheol.* **34** 553
[48] Schöpe H-J, Decker T and Palberg T 1998 *J. Chem. Phys.* **109** 10 068
[49] Palberg T, Mönch W, Schwarz J and Leiderer P 1995 *J. Chem. Phys.* **102** 5082
[50] Poon W C K 1998 *Curr. Opn Colloid Interface Sci.* **3** 593
[51] Van de Hulst H C 1981 *Light Scattering by Small Particles* (New York: Dover)
[52] Dhont J K G 1996 *An Introduction to the Dynamics of Colloids* (Amsterdam: Elsevier)
[53] Berne B and Pecora A 1990 *Dynamic Light Scattering* (Malaba: Krieger)
[54] Glatter O and Kratky O (eds) 1982 *Small Angle X-ray Scattering* (London: Academic)
[55] Ishimaru A 1978 *Wave Propagation and Scattering in Random Media* (New York: Academic)
[56] Born M and Wolf E 1975 *Principles of Optics* (Oxford: Pergamon) p 400

[57] Heymann A, Stipp A and Schätzel K 1994 *Nuovo Cimento* D **16** 1149
[58] Hünerbein S v, Würth M and Palberg T 1996 *Prog. Colloid Polym. Sci.* **100** 241
[59] Palberg T and Streicher K 1994 *Nature* **367** 51
[60] Bartlett P, Ottewill R H and Pusey P N 1990 *J. Chem. Phys.* **93** 1299
[61] Gast A P and Monovoukas Y 1991 *Nature* **351** 553
[62] Dux Chr and Versmold H 1997 *Phys. Rev. Lett.* **78** 1811
[63] Laun H M, Bung R, Hess S, Loose W, Hess O, Hahn K, Hädicke E, Hingmann R, Schmidt F and Lindner P 1993 *J. Rheol.* **36** 1057
[64] Dux Ch, Musa S, Reus V, Versmold H, Schwahn D and Lindner P 1998 *J. Chem. Phys.* **109** 2556
[65] Heymann A 1997 *PhD Thesis* Kiel
[66] Heymann A, Stipp A, Sinn Chr and Palberg T 1998 *J. Colloid Interface Sci.* **206** 119
[67] Palberg T, Härtl W, Wittig U, Versmold H, Würth M and Simnacher E 1992 *J. Phys. Chem.* **96** 8180
[68] Harland J L and van Megen W 1996 *Phys. Rev.* E **55** 3054
[69] James R W 1965 *Optical Principles of Diffraction of X-Rays* ed L Bragg (Ithaca: Cornell University Press)
[70] Schätzel K and Ackerson B J 1993 *Phys. Rev.* E **48** 3766
[71] Furukawa H 1984 *Physica* A **123** 497
[72] He Y, Ackerson B J, van Megen W, Underwood S M and Schätzel K 1996 *Phys. Rev.* E **54** 5286
[73] Ackerson B J and Schätzel K 1995 *Phys. Rev.* E **52** 6448
[74] Russel W B, Chaikin P M, Zhu J, Meyer W V and Rogers R 1997 *Langmuir* **13** 3871
[75] Derber S, Palberg T, Schätzel K and Vogel J 1997 *Physica* A **235** 204
[76] Sinn C, Stipp A, Heymann A and Palberg T unpublished
[77] Murray C A and Grier D G 1996 *Annu. Rev. Phys. Chem.* **47** 421
[78] 1985 Proc. 'Atelier d'Hiver sur les Cristeaux Colloideaux (Les Houches 1985) *J. Physique Coll.* **46** C3
[79] Elliot M S, Bristol B T F and Poon W C K 1997 *Physica* A **235** 216
[80] Verhaegh N A M, van Duijneveldt J S, van Blaaderen A and Lekkerkerker H N W 1995 *J. Chem. Phys.* **102** 1416
[81] Rundquist P A, Photinos P, Jagannathan S and Asher S A 1989 *J. Chem. Phys.* **91** 4932
[82] Monovoukas Y and Gast A P 1990 *Phase Transitions* **21** 183
[83] Aastuen D J W, Clark N A, Kotter L K and Ackerson B J 1986 *Phys. Rev. Lett.* **57** 1733
Aastuen D J W, Clark N A, Kotter L K and Ackerson B J 1986 *Phys. Rev. Lett.* **57** 2772
[84] Okubo T 1994 *Macro-ion Characterization: from Dilute Solution to Complex Fluids (ACS Symposium Series 548)* ed K S Schmitz, p 364
[85] He Y, Olivier B and Ackerson B J 1997 *Langmuir* **13** 1408
[86] Maaroufi M R, Stipp A and Palberg T 1998 *Prog. Colloid Polym. Sci.* **108** 83
[87] Preis T, Biehl R and Palberg T 1998 *Prog. Colloid Polym. Sci.* **108** 129
[88] Würth M, Schwarz J, Culis F, Leiderer P and Palberg T 1995 *Phys. Rev.* E **52** 6415–23
[89] Phan S-E, Russel W B, Cheng Z, Zhu J, Chaikin P M, Dunsmuir J H and Ottewill R H 1996 *Phys. Rev.* E **54** 6633
[90] Bartsch E 1995 *Transport Theory Stat. Phys.* **24** 1125
[91] Dingenouts N, Norhausen Ch and Ballauff M 1998 *Macromolecules* **31** 8912
[92] Paulin S E, Ackerson B J and Wolfe M S 1996 *J. Colloid Interface Sci.* **178** 251
[93] Carnahan N F and Starling K E 1979 *J. Chem. Phys.* **51** 635
[94] Hall K R 1972 *J. Chem. Phys.* **57** 2252
[95] Bolhuis P G and Kofke D A 1994 *Phys. Rev.* E **54** 634
[96] Bartlett P 1997 *J. Chem. Phys.* **107** 186
[97] Courtemanche D J and van Swol F 1992 *Phys. Rev. Lett.* **69** 2078
[98] Neser S, Bechinger C, Leiderer P and Palberg T 1997 *Phys. Rev. Lett.* **79** 2348
[99] Frenkel D and Ladd A J C 1984 *J. Chem. Phys.* **81** 3188
[100] Woodcock L V 1997 *Nature* **384** 141
[101] Bruce A D, Wilding N B and Ackland G J 1997 *Phys. Rev. Lett.* **79** 3002
[102] Bartlett P, Pusey P N and Ottewill R H 1991 *Langmuir* **7** 213
[103] Davis K E, Russel W B and Glantschnig W J 1991 *J. Chem. Soc. Faraday Trans.* **87** 411
[104] van Blaaderen A, Ruel R and Wiltzius P 1997 *Nature* **385** 321
[105] Ackerson B J, Paulin S E, Johnson B, van Megen W and Underwood S 1998 *Phys. Rev.* E at press
[106] van Duijneveldt J S, Dhont J K G and Lekkerkerker H N W 1993 *J. Chem. Phys.* **99** 6941
[107] Henderson S I, Mortensen T C, Underwood S M and van Megen W 1996 *Physica* A **233** 102
[108] Dhont J K G, Smits C and Lekkerkerker H N W 1992 *J. Colloid Interface Sci.* **152** 386
[109] Schätzel K and Ackerson B J 1992 *Phys. Rev. Lett.* **68** 337
[110] van Megen W and Ackerson B J 1997 *Prog. Colloid Polym. Sci.* **104** 97

[111] Harland J L, Henderson S I, Underwood S M and van Megen W 1995 *Phys. Rev. Lett.* **75** 3572
[112] Heymann A, Sinn Chr and Palberg T 1998 *J. Chem. Phys.* submitted
[113] Marr D W M 1995 *J. Chem. Phys.* **102** 8283
[114] Lange H 1995 *Part. Part. Syst. Charact.* **12** 148
[115] Garbow N, Müller J, Schätzel K and Palberg T 1997 *Physica* A **235** 291
[116] Wittig U 1990 *PhD Thesis* Aachen
[117] Alexander S, Chaikin P M, Grant P, Morales G J, Pincus P and Hone D 1984 *J. Chem. Phys.* **80** 5776
[118] Stevens M J, Falk M L and Robbins M O 1996 *J. Chem. Phys.* **104** 5209
[119] Evers M, Garbow N, Hessinger D and Palberg T 1998 *Phys. Rev.* E **57** 6774
[120] Belloni L 1998 *Colloids Surf.* A **140** 227
[121] Palberg T, Härtl W, Deggelmann M, Simnacher E and Weber R 1991 *Prog. Colloid Polym. Sci.* **84** 352
[122] Krause R, Dáguanno B, Mendez-Alcaraz J M, Nägele G, Klein R and Weber R 1991 *J. Phys. F: Met. Phys.* **3** 4459
[123] Tata B V R, Rajalakshmi M and Arora A K 1992 *Phys. Rev. Lett.* **69** 3778
Palberg T and Würth M 1994 *Phys. Rev. Lett.* **72** 786
Tata B V R, Rajalakshmi M and Arova A K 1992 *Phys. Rev. Lett.* **72** 787
[124] Piazza R and Degiorgio V 1992 *Physica* A **182** 576
[125] Sirota E B, Ou-Yang H D, Sinha S K, Chaikin P M, Axe J D and Fujii Y 1989 *Phys. Rev. Lett.* **62** 1524
[126] Luck W, Klier M and Wesslau H 1963 *Ber. Bunsenges. Phys. Chem.* **67** 75
[127] Monovoukas Y and Gast A P 1989 *J. Colloid Interface Sci.* **128** 533
[128] Palberg T, Mönch W, Bitzer F, Bellini L and Piazza R 1995 *Phys. Rev. Lett.* **74** 4555
[129] Meijer E J and Frenkel D 1991 *J. Chem. Phys.* **94** 2269
[130] Voegtli L P and Zukoski C F IV 1991 *J. Colloid Interface Sci.* **141** 79
[131] Kesavamoorthy R, Sood A K, Tata B V R and Arora A K 1988 *J. Phys. C: Solid State Phys.* **21** 4737
[132] Härtl W, Versmold H and Zhang-Haider X 1995 *J. Chem. Phys.* **102** 6613
[133] Lai S K, Ma W J, van Megen W and Snook I K 1997 *Phys. Rev.* E **56** 766
[134] Meller A and Stavans J 1992 *Phys. Rev. Lett.* **68** 3645
[135] Imhof A and Dhont J K G 1995 *Phys. Rev.* B **52** 6344
[136] Yoshida H, Yamanaka J, Koga T, Ise N and Hashimoto T 1998 *Langmuir* **14** 569
[137] Larsen A E and Grier D G 1996 *Phys. Rev. Lett.* **76** 3862
[138] Arora A K (ed) 1995 *Ordering and Phase Transitions in Colloidal Systems* (New York: VCH)
[139] Graf H and Löwen H 1998 *Phys. Rev.* B **57** 5744
[140] Bucci S, Fagotti C, Degiorgio V and Piazza R 1991 *Langmuir* **7** 824
[141] Hug J E, van Swol F and Zukoski F 1995 *Langmuir* **11** 111
[142] Grier D G and Murray C A 1994 *J. Chem. Phys.* **100** 9088
[143] Ackerson B J 1983 *Physica* A **128** 221
[144] Paulin S E, Ackerson B J and Wolfe M S 1997 *Phys. Rev.* E **55** 5812
[145] Haw M D, Poon W C K and Pusey P N 1998 *Phys. Rev.* E **57** 6859
[146] Löwen H, Simon R and Palberg T 1993 *Phys. Rev. Lett.* **70** 1557
[147] Bitzer F, Palberg T, Löwen H, Simon R and Leiderer P 1994 *Phys. Rev.* E **50** 2821